

GRASSMANNIAN DIFFUSION MAPS BASED DIMENSION REDUCTION AND CLASSIFICATION FOR HIGH-DIMENSIONAL DATA *

KETSON R. M. DOS SANTOS[†], DIMITRIOS G. GIOVANIS[†], AND MICHAEL D. SHIELDS[†]

Abstract. Diffusion Maps is a nonlinear dimensionality reduction technique used to embed high-dimensional data in a low-dimensional Euclidean space where the notion of distance is due to the transition probability of a random walk over the dataset. However, the conventional approach is not capable to reveal the underlying subspace structure hidden in the same dataset, a useful information for machine learning applications such as object classification and facial recognition. To circumvent this limitation, a novel nonlinear dimensionality reduction technique, referred to as Grassmannian Diffusion Maps, is developed herein relying on the affinity between subspaces represented by points on the Grassmann manifold. To this aim, the elements of a dataset are projected onto a low-dimensional Grassmann manifold where the subspace structure of each data point is revealed. Next, given a graph on the Grassmann manifold, a kernel matrix encoding the affinity between connected subspaces is obtained to define the transition probability of the random walk over the dataset via the graph Laplacian normalization. Therefore, one can reveal the nonlinear structure of the Grassmann manifold from the eigendecomposition of the transition matrix. In this paper, three examples are used to evaluate the performance of both conventional and Grassmannian Diffusion Maps. First, a “toy” example shows that the Grassmannian Diffusion Maps can identify a well-defined parametrization of points on the unit sphere, representing a Grassmann manifold. The second example shows that the Grassmannian Diffusion Maps outperforms the conventional Diffusion Maps in classifying elements, later recovered by a conventional clustering, of a dataset by their intrinsic characteristics. In the last example, a novel classification/recognition technique is developed based on the theory of sparse representation. This method incorporates the ability of the Grassmannian Diffusion Maps in revealing the underlying subspace structure of a dataset to create an overcomplete dictionary of reduced dimension, whose atoms are given by the diffusion coordinates. Therefore, a compact and sparse solution of an underdetermined linear system is obtained solving a l_1 -norm minimization problem and is used to indicate the linear span of the training samples in a given class. An indicative example consists in the recognition of face images subject to varying illumination conditions, changes in face expressions, and occurrence of occlusions. The technique presented high recognition rates (i.e., 95% in the best-case scenario) using a fraction of the data required by conventional methods.

Key words. Grassmann manifold, diffusion maps, dimension reduction, data classification, face recognition

AMS subject classifications. 58D15, 58D10, 53B20, 53B21

1. Introduction. Dimensionality reduction techniques play a fundamental role in the interpretation and characterization of high-dimensional data used in computationally intensive data-driven applications such as data compression [30, 5, 18], data classification [19, 60, 61], uncertainty quantification [20, 47, 21, 57], and biological sciences [53, 40, 39], just to mention few of them. Although linear dimensionality reduction methods (e.g., principal component analysis (PCA) [31]) suffice to extract features of the elements of a dataset, they fail to capture the intrinsic nonlinear geometric structure of the dataset itself. To circumvent this limitation, kernel-based techniques have been successfully employed in several applications taking advantage of the data similarity expressed on a connected graph designed over the dataset. Among these techniques one can include isometric mapping, also known as Isomap [50, 3], Local Linear Embedding (LLE) [45, 15], T-distributed Stochastic Neighbor Embed-

*Preprint submitted to SIAM Journal of Scientific Computing.

[†]Department of Civil & Systems Engineering, Johns Hopkins University, Baltimore, MD, 21218, USA.

ding (t-SNE) [54], kernel principal component analysis (kernel PCA) [46]; Laplacian Eigenmaps [8], and Diffusion Maps [12, 11].

The objective of many nonlinear dimensionality reduction techniques is to project the data onto a low-dimensional manifold. One of the main advantages of this approach is that redundant and unimportant information can be identified and properly discarded. One such manifold, the Grassmann manifold [22, 62], a complete and connected smooth Riemannian manifold endowed with a metric, provides the mathematical tools to extract only the necessary information utilized in the characterization of high-dimensional data in a low-dimensional space. Grassmann manifold projection is a pointwise dimensionality reduction where the underlying orthogonal subspace of each element of a dataset is represented as a point on the Grassmann manifold. Several applications using Grassmann manifold projections are found in the literature including the works by Turaga et al. [51], where statistical inference on the manifold is investigated to improve the performance of techniques for activity recognition, video-based face recognition, and shape classification. Moreover, Harandi et al. [26] used the Grassmann manifold theory to address problems in sparse coding and dictionary learning, in particular the embedding of the manifold into the space of symmetric matrices. Giovanis and Shields [20, 21] introduced a computationally efficient surrogate modeling scheme based on Grassmann manifold projections for prediction of high-dimensional stochastic models in a uncertainty quantification perspective. Further, Zhang et al. [64] has shown that well-known learning techniques, including deep learning, can be exploited in a Grassmannian perspective of discriminant analysis, high-dimensional data clustering, and low-rank matrix completion. For video-based image set classification, Wang et al. [57] assumed that video sequences can be modeled as linear subspaces lying on a Grassmann manifold, where the graph embedding multi-kernel metric learning algorithm is employed in the measurement of dissimilarities for classification purposes.

Herein, a novel dimensionality reduction technique is introduced to reveal the global intrinsic structure of a dataset based on the underlying geometric structure of each data point. The technique has two steps, the first is a linear pointwise dimensionality reduction of each element of the dataset via their Grassmann manifold projections, where the redundant and unimportant features are discarded. The second step is a nonlinear dimension reduction aimed at learning the geometric structure of the Grassmann manifold on which the data lies. This uses the Diffusion Maps to perform the spectral characterization of a random walk over the dataset projected onto the Grassmann manifold. In the end, a set of coordinates in a Euclidean space, also known as diffusion coordinates, are determined based on the transition probability of the random walk to move from one state on the manifold to another. In comparison with existing techniques, this novel approach does not need to perform a global dimensionality reduction to identify the basis spanning all the elements of a given dataset. Moreover, the similarity between points in the dataset is defined by the affinity between their underlying subspaces. It has the advantage that the intrinsic geometry of each element, and not their topology in the ambient space, is considered and therefore more robust classifiers can be obtained. In this regard, the performance of the diffusion maps (DM) in several applications, such as facial recognition and object classification, can be enhanced.

This paper is organized as follows. In section 2, elements Grassmann manifold theory are introduced. The definitions of Stiefel and Grassmann manifolds are presented together with the definition of the tangent space and geodesic path, as well as definitions of the exponential and logarithmic maps. In section 3, the notion of

distance is introduced based on the concept of principal angles between subspaces. Section 4 introduces the concept of a kernel on the Grassmann manifold, which is necessary for the development of the multipoint dimensionality reduction. In section 5, the Grassmannian diffusion maps (GDM) is introduced and the characteristics of the obtained diffusion coordinates are discussed. Section 6 introduces a novel data classification technique where the sparse representation-based classification method [59] is informed by the Grassmannian diffusion maps and data classification can be performed with a fraction of the amount of data used by some conventional techniques. In section 7, three examples are presented to corroborate the arguments presented in sections 5 and 6 and to assess the performance of the conventional and the Grassmannian diffusion maps. The first example illustrates the ability of the GDM to reveal the structure of data projected on the Grassmann manifold through a simple, and easy-to-visualize, example of data generated on a structured nonlinear manifold. The second problem shows that, indeed the GDM has the ability to use the most important features of the data for classification. In the third example, the method is applied for facial recognition showing that it can be applied in practical applications.

2. Grassmann manifold. The theory of Grassmann manifolds contains the necessary elements to support the development of a diffusion maps technique based on appropriate Grassmannian kernels. In this section, such elements are exploited to describe two important manifolds, namely the Stiefel and Grassmann manifolds. In this regard, let's consider the ambient space \mathbb{R}^n where one can define a p -plane as the subspace of dimension p with $0 < p < n$, and a p -frame as an ordered set of p mutually orthonormal vectors in \mathbb{R}^n [2, 62]. The Stiefel manifold $\mathcal{V}(p, n)$, which is induced by the orthogonal group $O(n)$ [2], is defined as follows.

DEFINITION 2.1. *The Stiefel manifold $\mathcal{V}(p, n)$ is the set of p -frames in \mathbb{R}^n such that $\mathcal{V}(p, n) = \{\mathbf{X} \in \mathbb{R}^{n \times p} : \mathbf{X}^T \mathbf{X} = \mathbf{I}_p\}$.*

where $\mathbf{I}_p \in \mathbb{R}^{p \times p}$ is the identity matrix and $\mathbf{X} \in \mathbb{R}^{n \times p}$ is an orthonormal matrix. Moreover, $\mathcal{V}(p, n)$ is a compact manifold with dimension given by $\dim[\mathcal{V}(p, n)] = np - \frac{1}{2}p(p+1)$ [62]. Furthermore, the Stiefel manifold is a homogeneous space represented as a quotient space [62, 63, 35], such that

$$(2.1) \quad \mathcal{V}(p, n) \cong \frac{O(n)}{O(n-p)}.$$

The right action of $O(p)$ on $\mathcal{V}(p, n)$ induces a homogeneous space with dimension $p(n-p)$ known as the Grassmann manifold [62], whose definition is given next.

DEFINITION 2.2. *The Grassmann manifold (or Grassmannian) $\mathcal{G}(p, n)$ is a set of p -planes in \mathbb{R}^n where a point on $\mathcal{G}(p, n)$ is given by $\mathcal{X} = \text{span}(\Psi)$ with $\Psi \in \mathcal{V}(p, n)$.*

Moreover, \mathcal{X} is identified as an equivalence class of $n \times p$ matrices under orthogonal transformation of the Stiefel manifold [62, 63, 35], such that.

$$(2.2) \quad \mathcal{G}(p, n) \cong \frac{O(n)}{O(n-p)O(p)} = \frac{\mathcal{V}(p, n)}{O(p)}.$$

For $p = 1$ the Grassmann manifold $\mathcal{G}(1, n)$ is a generalization of the projective space \mathbb{P}^{n-1} corresponding to the lines passing through the origin of the Euclidean space [27]. Further, a point $\mathcal{X} = \text{span}(\Psi) \in \mathcal{G}(p, n)$ is invariant to the choice of basis such that $\text{span}(\Psi) = \text{span}(\mathbf{R}\Psi)$, where $\mathbf{R} \in SO(p)$, where $SO(p)$ is the special orthogonal group [62]. Herein, a point on the Grassmann manifold is an equivalence

class defined by a point on the Stiefel manifold. Therefore, a representation of a point on the Grassmann manifold is given by an orthonormal matrix $\Psi \in \mathbb{R}^{n \times p}$.

2.1. Grassmann manifold: Tangent space and geodesic path. Due to the smoothness of $\mathcal{G}(p, n)$ one can define tangent vectors at a given point $\mathcal{X} \in \mathcal{G}(p, n)$ as an equivalence class of differentiable curves $\gamma(t)$ passing through \mathcal{X} . In this regard, a tangent space $\mathcal{T}_{\mathcal{X}}\mathcal{G}(p, n)$, which is a flat inner-product space, is defined as follows [37, 56, 48].

DEFINITION 2.3. *The tangent space $\mathcal{T}_{\mathcal{X}}\mathcal{G}(p, n)$ is the a set of all tangent vectors in \mathcal{X} , such that*

$$(2.3) \quad \mathcal{T}_{\mathcal{X}}\mathcal{G}(p, n) = \{\mathbf{\Gamma} \in \mathbb{R}^{n \times p} : \mathbf{\Gamma}^T \Psi = \mathbf{0}\}.$$

Moreover, the geodesic curve $\gamma(t)$ on $\mathcal{G}(p, n)$ has the following definition

DEFINITION 2.4. *The geodesic curve $\gamma(t) : I \rightarrow \mathcal{G}(p, n)$, is a differentiable curve on $\mathcal{G}(p, n)$ that is locally length-minimizing with respect to a Riemannian metric.*

where I is an interval in \mathbb{R} . Further, the vectors tangent to $\gamma(t)$ are covariantly constant, where $\nabla_{\dot{\gamma}}\dot{\gamma}(t) = 0$ [14, 65].

To develop a map from the manifold to the tangent space and vice-versa let's first restrict the interval $I \in \mathbb{R}$ to $I = [0, t]$ yielding a geodesic segment joining $\gamma(0)$ to $\gamma(t)$. Therefore, using the Einstein summation convention and the Levi-Civita connection, one can make the covariant derivative of $\dot{\gamma}$ equal to zero [28, 14, 48], such that

$$(2.4) \quad \nabla_{\dot{\gamma}}\dot{\gamma}(t) = (\ddot{\gamma}^\lambda + \Gamma_{\mu\nu}^\lambda \dot{\gamma}^\mu \dot{\gamma}^\nu) \frac{\partial}{\partial \gamma^\lambda} = 0,$$

from where one can obtain the geodesic equation

$$(2.5) \quad \ddot{\gamma}^\lambda + \Gamma_{\mu\nu}^\lambda \dot{\gamma}^\mu \dot{\gamma}^\nu = 0,$$

where $\Gamma_{\mu\nu}^\lambda$ are the Christoffel symbols. Thus, due to the local existence and uniqueness theorem for geodesics, one can say that given a point $\mathcal{X}_0 \in \mathcal{G}(p, n)$ and a vector $\dot{\mathcal{X}}_0 \in \mathcal{T}_{\mathcal{X}_0}\mathcal{G}(p, n)$ the geodesic exists and it is unique, such that $\gamma(0) = \mathcal{X}_0$ and $\dot{\gamma}(0) = \dot{\mathcal{X}}_0$. This can be proven using the theory of ordinary differential equations [28, 14, 44].

2.2. Grassmann manifold: exponential and logarithmic maps. Considering that the Grassmann manifold $\mathcal{G}(p, n)$ is connected and complete as a metric space, one can define an exponential map $\exp_{\mathcal{X}} : \mathcal{T}_{\mathcal{X}}\mathcal{G}(p, n) \rightarrow \mathcal{G}(p, n)$ from the tangent space to every point $\mathcal{X} \in \mathcal{G}(p, n)$. Consider two points $\mathcal{X}_0 = \text{span}(\Psi_0)$ and $\mathcal{X}_1 = \text{span}(\Psi_1)$ in $\mathcal{G}(p, n)$, and a tangent space $\mathcal{T}_{\mathcal{X}_0}\mathcal{G}(p, n)$ with $\mathbf{\Gamma} \in \mathcal{T}_{\mathcal{X}_0}\mathcal{G}(p, n)$; one can map $\mathbf{\Gamma}$ to $\gamma(1) = \mathcal{X}_1$, where $\gamma(0) = \mathcal{X}_0$ and $\dot{\gamma}(0) = \dot{\mathcal{X}}_0$ (see Fig. 1) [20, 48]. Letting \mathcal{X}_1 be expressed by the orthonormal matrix Ψ_1 , the exponential map can be written as:

$$(2.6) \quad \exp_{\mathcal{X}_0}(\mathbf{\Gamma}) = \Psi_1.$$

Expressing $\mathbf{\Gamma}$ by its thin singular value decomposition $\mathbf{\Gamma} = \mathbf{USV}^T$ one can write Ψ_1 as

$$(2.7) \quad \Psi_1 = \exp_{\mathcal{X}_0}(\mathbf{USV}^T) = \Psi_0 \mathbf{V} \cos(\mathbf{S}) \mathbf{Q}^T + \mathbf{U} \sin(\mathbf{S}) \mathbf{Q}^T,$$

where $\mathbf{Q} \in \mathbb{R}^{n \times n}$ is an orthogonal matrix satisfying the following expressions.

$$(2.8) \quad \mathbf{V} \cos(\mathbf{S}) \mathbf{Q}^T = \Psi_0^T \Psi_1,$$

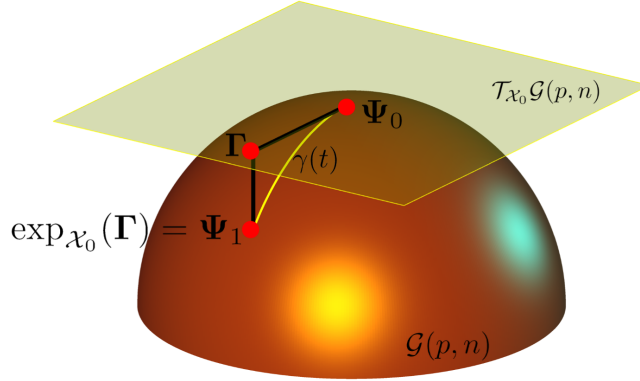


Figure 1: Exponential map of a point $\Gamma \in \mathcal{T}_{\mathcal{X}}\mathcal{G}(1, 3)$ to the Grassmann manifold $\mathcal{G}(1, 3)$.

and

$$(2.9) \quad \mathbf{U} \sin(\mathbf{S}) \mathbf{Q}^T = \Psi_1 - \Psi_0 \Psi_0^T \Psi_1.$$

Multiplying Eq. (2.9) by the inverse of the right-hand side of Eq. (2.8) one can obtain the following expression.

$$(2.10) \quad \mathbf{U} \tan(\mathbf{S}) \mathbf{V}^T = (\Psi_1 - \Psi_0 \Psi_0^T \Psi_1) (\Psi_0^T \Psi_1)^{-1}.$$

Thus, if we define the matrix $\mathbf{M} = (\Psi_1 - \Psi_0 \Psi_0^T \Psi_1) (\Psi_0^T \Psi_1)^{-1}$ and express its thin SVD by $\mathbf{M} = \mathbf{U} \mathbf{S} \mathbf{V}^T$, the logarithmic map $\log_{\mathcal{X}} : \mathcal{G}(p, n) \rightarrow \mathcal{T}_{\mathcal{X}}\mathcal{G}(p, n)$, which is only invertible in the area close to \mathcal{X}_0 [48], is given by

$$(2.11) \quad \log_{\mathcal{X}}(\Psi_1) = \mathbf{U} \tan^{-1}(\mathbf{S}) \mathbf{V}^T.$$

The geodesic $\gamma(t)$ parameterizes the curve connecting Ψ_0 and Ψ_1 on $t \in [0, 1]$ with $\gamma(0) = \Psi_0$ and $\gamma(1) = \Psi_1$ such that their respective projections in the tangent space are connected by a straight line. It can thus be represented by the projection of this line in the tangent space by the exponential mapping where Γ is expressed by its thin singular value decomposition $\Gamma = \mathbf{U} \mathbf{S} \mathbf{V}^T$ [6]. Therefore, one can write $\gamma(t)$ as

$$(2.12) \quad \gamma(t) = \text{span} [(\Psi_0 \mathbf{V} \cos(t\mathbf{S}) + \mathbf{U} \sin(t\mathbf{S})) \mathbf{V}^T].$$

3. Distances and metrics on the Grassmann manifold. Points on the Grassmann manifold are intrinsically connected by smooth curves along which one can define a proper notion of distance. These distances are measured through the principal angles of the distance between the subspaces representing points on the Grassmann manifold, defined as follows.

DEFINITION 3.1. *Considering $\mathbf{u}_i \in \text{span}(\Psi_u)$ and $\mathbf{v}_i \in \text{span}(\Psi_v)$ on $\mathcal{G}(k, n)$ and $\mathcal{G}(l, n)$, respectively, and letting $p = \min(k, l)$; the principal angles $0 \leq \theta_1 \leq \theta_2 \leq \dots \leq \theta_p \leq \pi/2$ are recursively obtained from $\cos(\theta_i) = \max_{\mathbf{u}_i} \max_{\mathbf{v}_i} \mathbf{u}_i^T \mathbf{v}_i$ where \mathbf{u}_i and \mathbf{v}_i are orthonormal vectors.*

Alternatively, the cosine of the principal angles $\theta_i \in [0, \pi/2]$ between the subspaces $\text{span}(\Psi_u)$ and $\text{span}(\Psi_v)$ can be computed from the singular values of $\Psi_u^T \Psi_v$. In this regard, one can write that

$$(3.1) \quad \Psi_u^T \Psi_v = \bar{\mathbf{U}} \bar{\mathbf{S}} \bar{\mathbf{V}}^T,$$

where $\bar{\mathbf{U}} \in O(k)$, $\bar{\mathbf{V}} \in O(l)$, and $\bar{\mathbf{S}} = \text{diag}(\sigma_1, \sigma_2, \dots, \sigma_p)$, with $p = \min(k, l)$. Thus, the principal angles are computed as $\theta_i = \cos^{-1}(\sigma_i)$ [38].

In fact, it has been shown that any measure of distance on the Grassmann manifold must be a function of the principal angles as stated in the following theorem (repeated from [58, 63]).

THEOREM 3.2. *Any notion of distance between k -dimensional subspaces in \mathbb{R}^n that depends only on the relative positions of the subspaces, i.e., invariant under any rotation in $O(n)$, must be a function of their principal angles. To be more specific, if a distance $d : \mathcal{G}(k, n) \times \mathcal{G}(k, n) \rightarrow [0, \infty)$ satisfies $d(Q \cdot \Psi_0, Q \cdot \Psi_1) = d(\Psi_0, \Psi_1)$ for all $d(\Psi_0, \Psi_1) \in \mathcal{G}(k, n)$ and all $Q \in O(n)$, where $Q \cdot \Psi_0 := \text{span}(Q\Psi_0) \in \mathcal{G}(k, n)$, then d must be a function of $\theta_i(\Psi_0, \Psi_1), i = 1, \dots, k$.*

Perhaps the most common distance, the geodesic distance $d_{\mathcal{G}(p,n)}(\Psi_0, \Psi_1)$ between two points $\mathcal{X}_0 = \text{span}(\Psi_0)$ and $\mathcal{X}_1 = \text{span}(\Psi_1)$ on $\mathcal{G}(p, n)$, corresponds to the distance over the geodesic $\gamma(t)$ parameterized by $t \in [0, 1]$ and it is given by [58, 62, 20]

$$(3.2) \quad d_{\mathcal{G}(p,n)}(\Psi_0, \Psi_1) = \|\Theta\|_2,$$

where $\Theta = (\theta_1, \theta_2, \dots, \theta_p)$ is the vector of principal angles. This notion of distance, using the arc-length metric, between two subspaces in $\mathcal{G}(2, 3)$ is represented in the unit semi-sphere in Fig. 2. Several definitions of distance on $\mathcal{G}(p, n)$ can be found in the literature (see [62] for detailed information) and are listed in Table 1.

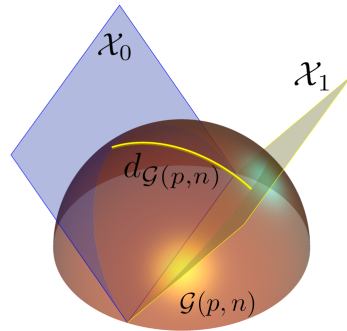


Figure 2: Geodesic distance between subspaces \mathcal{X}_0 and \mathcal{X}_1 of \mathbb{R}^2 on $\mathcal{G}(2, 3)$.

Table 1: Distances and metrics on the Grassmann manifold

	<i>Principal angles</i>	<i>Orthonormal basis</i>	<i>Metric</i>
Asimov	θ_p	$\cos^{-1} \ \Psi_0^T \Psi_1\ _2$	yes
Binet-Cauchy	$(1 - \prod_{i=1}^p \cos^2 \theta_i)^{1/2}$	$[1 - (\det \Psi_0^T \Psi_1)^2]^{1/2}$	yes
Arc-length	$(\sum_{i=1}^p \theta_i)^{1/2}$	$\ \cos^{-1} \Sigma\ _F$	yes
Chordal	$(\sum_{i=1}^p \sin^2 \theta_i)^{1/2}$	$\frac{1}{\sqrt{2}} \ \Psi_0 \Psi_0^T - \Psi_1 \Psi_1^T\ _F$	yes
Fubini-Study	$\cos^{-1} (\prod_{i=1}^p \cos \theta_i)$	$\cos^{-1} \det \Psi_0^T \Psi_1 $	yes
Martin	$(\log \prod_{i=1}^p 1/\cos^2 \theta_i)^{1/2}$	$(-2 \log \det \Psi_0^T \Psi_1)^{1/2}$	yes
Procrustes	$(2 \sum_{i=1}^p \sin^2 \frac{\theta_i}{2})^{1/2}$	$\ \Psi_0 \mathbf{U} - \Psi_1 \mathbf{V}\ _F$	yes
Procrustes 2-norm	$2 \sin^2 \frac{\theta_p}{2}$	$\ \Psi_0 \mathbf{U} - \Psi_1 \mathbf{V}\ _2$	yes
Projection	$\sin \theta_p$	$\ \Psi_0 \Psi_0^T - \Psi_1 \Psi_1^T\ _2$	yes
Spectral	$2 \sin \frac{\theta_p}{2}$	$\ \Psi_0 \mathbf{U} - \Psi_1 \mathbf{V}\ _2$	yes
Mean distance	$\frac{1}{p} \sum_{i=1}^p \sin^2 \theta_i$	$\frac{1}{p\sqrt{2}} \ \Psi_0 \Psi_0^T - \Psi_1 \Psi_1^T\ _F^2$	yes
Max Correlation	$\sin \theta_1$	$\ (\Psi_0 \Psi_0^T - \Psi_1 \Psi_1^T)^{-1}\ _2$	no

When defining a distance, it is often important that the distance be provided in terms of a metric, which formalizes the notation of distance on the manifold, and is defined next.

DEFINITION 3.3. *A metric on the Grassmann manifold is a function $d : \mathcal{G}(k, n) \times \mathcal{G}(k, n) \rightarrow [0, \infty)$ where $[0, \infty)$ is the set of non-negative real numbers and for all $\mathcal{X}_0 = \text{span}(\Psi_0), \mathcal{X}_1 = \text{span}(\Psi_1), \mathcal{X}_2 = \text{span}(\Psi_2) \in \mathcal{G}(k, n)$, the following three conditions are satisfied:*

1. $d(\mathcal{X}_0, \mathcal{X}_1) = 0 \Leftrightarrow \mathcal{X}_0 = \mathcal{X}_1$ (*identity of indiscernibles*)
2. $d(\mathcal{X}_0, \mathcal{X}_1) = d(\mathcal{X}_1, \mathcal{X}_0)$ (*symmetry*)
3. $d(\mathcal{X}_0, \mathcal{X}_1) \leq d(\mathcal{X}_0, \mathcal{X}_2) + d(\mathcal{X}_2, \mathcal{X}_1)$ (*triangle inequality*)

The formalism of a metric on the manifold can be useful in properly defining a distance. This can be seen, for example, by observing that the value $\sin \theta_1$ is sometimes called the max correlation distance or spectral distance [63], but it is not a distance in the sense of a metric because it can be zero for a pair of distinct subspaces. Clearly this is undesirable.

4. Grassmannian kernels. The notion of a metric on the Grassmann manifold is useful as an assessment tool to evaluate the proximity of points (subspaces) on the manifold. However, it is not sufficient as a tool for achieving an additional dimension reduction on a collection of points on a manifold as is necessary, for example, for clustering and classification of points on the manifold. This additional dimension reduction requires embedding the points on the manifold into a higher-dimensional “feature” space (the so-called “kernel trick” common to many nonlinear dimension reduction methods). For this, a kernel is required. Next, we discuss the use of kernels on the Grassmann manifold.

The embedding of Grassmannians into Hilbert spaces, where a Euclidean structure is identified, can be performed using Grassmannian kernels. In this regard, one can resort to the following definition of real-valued positive semi-definite kernels.

DEFINITION 4.1. *A real symmetric map is a real-valued positive semi-definite kernel if $\sum_{i,j} c_i c_j k(x_i, x_j) \leq 0$, with $x \in \mathcal{X}$ and $c_i \in \mathbb{R}$.*

Therefore, a Grassmannian kernel can be defined as

DEFINITION 4.2. *A map $k : \mathcal{G}(p, n) \times \mathcal{G}(p, n) \rightarrow \mathbb{R}$ is a Grassmannian kernel if it is invariant to the choice of basis and positive semi-definite.*

In kernel-based dimensionality reduction techniques, there are many commonly used kernels defined on Euclidean spaces. The Gaussian kernel is perhaps the most popular and is given by,

$$(4.1) \quad k(\mathbf{X}_i, \mathbf{X}_j) = \exp\left(-\frac{\|\mathbf{X}_i - \mathbf{X}_j\|_2^2}{4\varepsilon}\right),$$

where \mathbf{X}_i and \mathbf{X}_j are data points in the ambient Euclidean space and ε is the parameter controlling the spread of the kernel tails. It could be tempting to simply substitute the Euclidean norm in the definition of the Gaussian kernel by a metric on the Grassmann manifold. However, this procedure yields a non positive semi-definite, although symmetric, kernel [27].

Several families of Grassmannian kernels, with different characteristics, are proposed in the literature (see [24, 25, 27]). However, the most popular positive semi-definite kernels are the Binet-Cauchy and Projection kernels. These kernels can be employed on the transformation of problems defined on the Grassmann manifold to problems on Hilbert spaces. Next, a detailed analysis of both kernels is presented.

4.1. Embedding the Grassmann manifold. The embedding of the Grassmann manifold into Hilbert spaces is analyzed herein. In particular, the Plücker and the projection embeddings are considered to show how to construct the the Binet-Cauchy and projection kernels, respectively.

4.1.1. Binet-Cauchy kernel: Plücker embedding. The Plücker embedding plays an important role in embedding the Grassmann manifold $\mathcal{G}(p, n)$ into the projective space $\mathbb{P}(\wedge^p \mathbb{R}^n)$, where the exterior product $\wedge^p \mathbf{V}$ is the k -th product of a vector space \mathbf{V} . Thus, the Plücker embedding $P : \mathcal{G}(p, n) \rightarrow \mathbb{P}(\wedge^p \mathbb{R}^n)$ can be defined as $P(\Psi) = [\psi_1 \wedge \psi_2 \wedge \dots \wedge \psi_p]$. One can easily show that the Plücker coordinates of $\Psi \in \mathcal{G}(p, n)$ are the $p \times p$ minors, matrices obtained by taking p rows out of n of \mathbf{X} . This property can be used to define a inner product over $\mathbb{P}(\wedge^p \mathbb{R}^n)$ by taking advantage of compound matrices, such that the elements of the q -th compound matrix $C_q(\Psi)$ of a matrix Ψ are the minors of Ψ of order q arranged in a lexicographic order [27]. Thus, using the Binet-Cauchy theorem [55, 27] and given the points $\mathcal{X}_0 = \text{span}(\Psi_0) \in \mathcal{G}(n, k)$ and $\mathcal{X}_1 = \text{span}(\Psi_1) \in \mathcal{G}(n, l)$, one can write $C_q(\Psi_0^T \Psi_1) = C_q(\Psi_0)^T C_q(\Psi_1)$. Therefore, $k_{bc}(\Psi_0, \Psi_1) = \text{Tr}[C_q(\Psi_0)^T C_q(\Psi_1)] = \text{Tr}[C_q(\Psi_0^T \Psi_1)] = \det(\Psi_0^T \Psi_1)$, which can be defined as an inner product for the Plücker embedding. One of the problems with this definition of inner product is that the sign of $\det(\cdot)$ can change when columns of Ψ_0 are permuted. This limitation can be circumvented by taking the square value of $\det(\Psi_0^T \Psi_1)$. Thus, one can write $k_{bc}(\Psi_0, \Psi_1) = \det(\Psi_0^T \Psi_1)^2$. In reality several families of kernels are constructed based on the Binet-Cauchy theorem. It includes the polynomial generalizations $k_{bc}(\Psi_0, \Psi_1) = [\beta + \det(\Psi_0^T \Psi_1)]^\alpha$ (see [27] for a detailed description). Herein, the adopted definition of the Binet-Cauchy kernel is given by

$$(4.2) \quad k_{bc}(\Psi_0, \Psi_1) = \det(\Psi_0^T \Psi_1)^2,$$

whose relation with the principal angles is given by [24, 27]

$$(4.3) \quad k_{bc}(\Psi_0, \Psi_1) = \prod_{i=1}^p \cos^2(\theta_i).$$

4.1.2. Projection kernel: projection embedding. The projection kernel is defined straightforwardly using the projection embedding $\Pi : \mathcal{G}(p, n) \rightarrow \mathbb{R}^{n \times n}$ given by $\Pi(\Psi) = \Psi\Psi^T$. This map corresponds to a diffeomorphism, a differentiable mapping with a continuous differentiable inverse, from the Grassmann manifold to the set of rank p symmetric orthogonal projection matrices. Therefore, a natural definition of inner product for the projection embedding is given by $\langle \Psi_0, \Psi_1 \rangle_{\Pi} = \text{Tr} \left[\Pi(\Psi_0)^T \Pi(\Psi_1) \right] = \|\Psi_0^T \Psi_1\|_F^2$. As for the Binet-Cauchy kernel, several families can be obtained using the projection embedding, however, herein the projection kernel is defined as

$$(4.4) \quad k_{pr}(\Psi_0, \Psi_1) = \|\Psi_0^T \Psi_1\|_F^2,$$

whose relation with the principal angles is given by [24, 27]

$$(4.5) \quad k_{pr}(\Psi_0, \Psi_1) = \sum_{i=1}^p \cos^2(\theta_i).$$

4.2. Grassmannian kernel dimensionality. The properties of the projection and Binet-Cauchy kernels that may have some influence on their selection for a specific application are investigated in this section. The relationship between the dimensionality of the Grassmann manifold $\mathcal{G}(p, n)$, and the entries of the kernel matrix, is analyzed based on the distribution of the principal angles between random matrices. In this regard, let's first assume $p = 1$ in Eqs. (4.2 - 4.5). One can easily show that $k_{pr}(\Psi_i, \Psi_j) = k_{bc}(\Psi_i, \Psi_j)$ for two different subspaces $\mathcal{X}_i = \text{span}(\Psi_i)$ and $\mathcal{X}_j = \text{span}(\Psi_j)$. However, more attention should be paid to the influence of p and n , when $1 < p < n$ and $n > 1$, in the similarity between distinct points in the same manifold. Next, a more detailed analysis is presented for both the projection and Binet-Cauchy kernels. Further, the lemmas presented in this section are developed considering two subspaces $\mathcal{X}_i = \text{span}(\Psi_i)$ and $\mathcal{X}_j = \text{span}(\Psi_j)$ chosen from the uniform distribution on $\mathcal{G}(p, n)$, which is an invariant distribution on the Grassmann manifold. Moreover, the entries of the kernel matrix are denoted by $k_{ij} = k(\Psi_i, \Psi_j)$, where for an ensemble of random subspaces the expected value is denoted by \bar{k}_{ij} .

4.2.1. Kernel dimensionality: projection kernel. The following lemmas are used to show that the expected values of the entries of the kernel matrix $k_{pr}(\Psi_i, \Psi_j)$ have a well-defined functional relationship with both p and n .

LEMMA 4.3. *Given two random subspaces $\mathcal{X}_i = \text{span}(\Psi_i)$ and $\mathcal{X}_j = \text{span}(\Psi_j)$ on $\mathcal{G}(p, n)$, if $i = j$ the entries in the diagonal of $k_{pr}(\Psi_i, \Psi_j)$ are given by $k_{ii} = p$.*

Proof. The proof of lemma 4.3 is trivial because $\cos^2(\theta_i) = 1$ for $i = 1, \dots, p$ in Eq. (4.5). \square

On the other hand, if $i \neq j$, the following lemma holds.

LEMMA 4.4. *Given two random subspaces $\mathcal{X}_i = \text{span}(\Psi_i)$ and $\mathcal{X}_j = \text{span}(\Psi_j)$ on $\mathcal{G}(p, n)$, if $1 \leq p \leq n$ the expected value $\bar{k}_{ij}(p, n)$ of the off-diagonal entries of*

$k_{pr}(\Psi_i, \Psi_j)$ has the following functional form

$$(4.6) \quad \bar{k}_{ij}(p, n) = \frac{p^2}{n}.$$

Proof. A fixed subspace $\mathcal{X}_i = \text{span}(\Psi_i)$ and a subspace $\mathcal{X}_j = \text{span}(\Psi_j)$ chosen from the uniform distribution on $\mathcal{G}(p, n)$, which is an invariant distribution on the Grassmann manifold, are given by

$$(4.7) \quad \Psi_i = \begin{bmatrix} \mathbf{I}_p \\ \mathbf{0}_{n-p,p} \end{bmatrix},$$

and

$$(4.8) \quad \hat{\Psi}_j = \begin{bmatrix} \mathbf{A} \\ \mathbf{B} \end{bmatrix},$$

where \mathbf{I}_p is a $p \times p$ identity matrix, $\mathbf{0}_{n-p,p}$ is a $(n-p) \times p$ null matrix, $\mathbf{A} \in \mathbb{R}^{p \times p}$ and $\mathbf{B} \in \mathbb{R}^{(n-p) \times p}$ are i.i.d. Gaussian matrices, since the Gaussian distribution is invariant under orthogonal group transformation [1]. Further, the orthonormalization of $\hat{\Psi}_j$ is given by $\Psi_j = \hat{\Psi}_j (\mathbf{A}^T \mathbf{A} + \mathbf{B}^T \mathbf{B})^{-1/2}$. Thus, $\sigma_i^2 = \cos^2(\theta_i)$, with $i = 1, \dots, p$, are equal to the eigenvalues values $\{\lambda_i\}_{i=1}^p$ of $(\mathbf{A}^T \mathbf{A} + \mathbf{B}^T \mathbf{B})^{-1/2} \mathbf{A}^T \mathbf{A} (\mathbf{A}^T \mathbf{A} + \mathbf{B}^T \mathbf{B})^{-1/2}$. Or equivalently given by the eigenvalues of $\mathbf{W} = (\mathbf{L}^{-1})^T \mathbf{A}^T \mathbf{A} \mathbf{L}^{-1}$, where $\mathbf{A}^T \mathbf{A} + \mathbf{B}^T \mathbf{B} = \mathbf{L}^T \mathbf{L}$ is the Cholesky decomposition of $\mathbf{A}^T \mathbf{A} + \mathbf{B}^T \mathbf{B}$. As \mathbf{L} has a beta distribution $\text{Beta}_p[p/2, (n-p)/2]$, the joint probability density function (PDF) of $\{\lambda_i\}_{i=1}^p$, when $n \geq 2p$, is given by [42, 17, 1]

$$(4.9) \quad f(\lambda_1, \dots, \lambda_p) = \frac{\pi^{p^2/2} \Gamma_p(n/2)}{\Gamma_p^2(p/2) \Gamma_p((n-p)/2)} \prod_{i < j} |\lambda_i - \lambda_j| \prod_{i=1}^p \lambda_i^{-1/2} (1 - \lambda_i)^{\frac{1}{2}(n-2p-1)},$$

where $\Gamma_m(\cdot)$ is the multivariate gamma function [42, 1]. Therefore, the PDF of the largest principal angle between the subspaces \mathcal{X}_i and \mathcal{X}_j randomly chosen from $\mathcal{G}(p, n)$ can be obtained (see [1] for a detailed presentation). At this point, our interest is focused on the case $p = 1$, whose PDF of the cosine square of the unique principal angle is given by

$$(4.10) \quad f(\lambda) = \frac{\Gamma\left(\frac{n}{2}\right)}{\Gamma\left(\frac{1}{2}\right) \Gamma\left(\frac{n-1}{2}\right)} \lambda^{-\frac{1}{2}} [1 - \lambda]^{\frac{n-3}{2}},$$

where $\Gamma(\cdot)$ is the gamma function, $\lambda = \cos^2(\theta_1)$. The mean and variance are given by

$$(4.11) \quad \mathbb{E}[\lambda] = \frac{1}{n},$$

and

$$(4.12) \quad \text{Var}[\lambda] = \frac{2(n-1)}{n^2(n+2)}.$$

Next, let's assume that $\Psi_i^T \Psi_j = \mathbf{U} \mathbf{S} \mathbf{V}$, where $\mathbf{S} = \text{diag}([\sigma_1, \dots, \sigma_p])$. Therefore, considering that Ψ_i and Ψ_j are orthonormal matrices, one can use the following identity

$$(4.13) \quad \sum_{i=1}^p \sigma_i^2 = \text{Tr}(\Psi_i \Psi_i^T \Psi_j \Psi_j^T).$$

Therefore, considering that $\mathbf{Z} = \Psi_i \Psi_i^T \Psi_j \Psi_j^T$ one can write Eq. (4.13) for every realization ξ of Ψ_j , such that

$$(4.14) \quad \sum_{i=1}^p \sigma_i^2(\xi) = \sum_{i=1}^p \mathbf{Z}_{ii}(\xi).$$

Taking the expectation of both sides of Eq. (4.14) and assuming that the expectation of a summation is the summation of the individual expectations, one can obtain

$$(4.15) \quad \sum_{i=1}^p \mathbb{E}[\sigma_i^2(\xi)] = \sum_{k=1}^p \mathbb{E}[\mathbf{Z}_{kk}(\xi)].$$

From the definition of \mathbf{Z} one can obtain

$$(4.16) \quad \mathbf{Z}_{kk}(\xi) = \sum_{l=1}^p \Psi_{j,(k,l)}^2,$$

where $\Psi_{j,(k,l)}$ corresponds to the element (k, l) of Ψ_j . Therefore, as the columns of Ψ_j are orthonormal vectors in \mathbb{R}^n , the components of the vector $\Psi_{j,(:,l)}$ are equal to the cosine of the direction angles α_k between Ψ_j and the component in the coordinate axis k with $k = 1, \dots, n$. It is clear that the dot product of unit vectors uniformly distributed on the sphere \mathbb{S}^n has a beta distribution; thus, assuming that $\Psi_{j,(k,l)}$ are i.i.d. one can find that $(\Psi_{j,(k,l)} + 1) / 2 \sim \text{Beta}[(n-1)/2, (n-1)/2]$ [23]. As $\mathbb{E}[\Psi_{j,(k,l)}] = 0$, the variance of $\Psi_{j,(k,l)}$ is given by

$$(4.17) \quad \text{Var}[\Psi_{j,(k,l)}] = \mathbb{E}[\Psi_{j,(k,l)}^2] = \frac{1}{n}.$$

Moreover, if the columns of Ψ_j are orthonormal vectors in \mathbb{R}^n , the components of the vector $\Psi_{j,(:,l)}$ are equal to the cosine of the direction angles α_k between Ψ_j and the component in the coordinate axis k with $k = 1, \dots, n$. Therefore, $\Psi_{j,(k,l)}^2 = \cos^2(\alpha_k)$. Thus, one can observe that the results presented in Eqs. (4.10 - 4.12) are valid for $\lambda = \cos^2(\alpha_k)$. Therefore, from Eq. (4.16) one can show that

$$(4.18) \quad \mathbb{E}[\mathbf{Z}_{kk}(\xi)] = \frac{p}{n}.$$

Substituting Eq. (4.18) in Eq. (4.15) one can easily show that

$$(4.19) \quad \bar{k}_{ij}(p, n) = \sum_{i=1}^p \mathbb{E}[\sigma_i^2(\xi)] = \frac{p^2}{n}. \quad \square$$

A Monte Carlo simulation is performed to verify the consistency of the result presented in this section. In this regard, 3,000 random matrices $\hat{\Psi}_j$ are sampled from a Gaussian distribution, as presented in the proof of lemma 4.4, for each value of $p = 1, \dots, 19$, with $n = 20$. Thus, it is shown in Fig. 3 that the result of lemma 4.4 holds.

4.2.2. Kernel dimensionality: Binet-Cauchy kernel. From Eq. (4.2) the Binet-Cauchy kernel corresponds to the product of the square of the singular values of $\Psi_i^T \Psi_j$. In this regard, the values of the off-diagonal elements of $k_{bc}(\Psi_i, \Psi_j)$ are governed by those singular values larger than zero and lower than one. Therefore, one can start this analysis assuming that the following lemma holds.

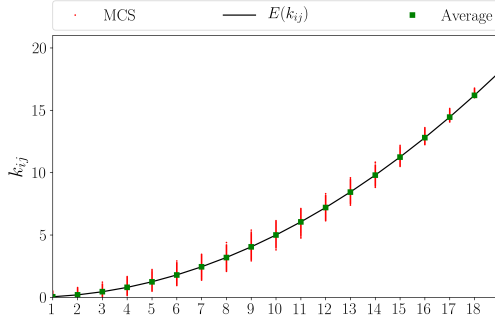


Figure 3: Average from the Monte Carlo simulation and the expected value of the off-diagonal elements of the projection kernel as a function of p for $n = 20$.

LEMMA 4.5. *Given two random subspaces \mathcal{X}_i and \mathcal{X}_j on $\mathcal{G}(p, n)$, if $p \geq n/2$ the multiplicity of the principal angle $\theta = 0$ between them is equal to $2p - n$.*

Proof. Assuming that $\mathcal{X}_i = \text{span}(\Psi_i)$ and $\mathcal{X}_j = \text{span}(\Psi_j)$ and considering that the multiplicity of the principal angle $\theta = 0$ between \mathcal{X}_i and \mathcal{X}_j is equal to $\dim(\mathcal{X}_i \cap \mathcal{X}_j)$ one can use the following expression

$$(4.20) \quad \dim(\mathcal{X}_i \cap \mathcal{X}_j) = \dim(\mathcal{X}_i) + \dim(\mathcal{X}_j) - \dim(\mathcal{X}_i + \mathcal{X}_j),$$

or alternatively,

$$(4.21) \quad \dim(\mathcal{X}_i \cap \mathcal{X}_j) = \text{rank}(\Psi_i) + \text{rank}(\Psi_j) - \text{rank}([\Psi_i, \Psi_j]). \quad \square$$

As $\mathcal{X}_i, \mathcal{X}_j \in \mathcal{G}(p, n)$, $\text{rank}(\Psi_i) = \text{rank}(\Psi_j) = p$. Moreover, $\text{rank}([\Psi_i, \Psi_j]) = n$, since $p \geq n/2$. Therefore, $\dim(\mathcal{X}_i \cap \mathcal{X}_j) = 2p - n$.

The result presented in lemma 4.5 is useful to show that $p = n/2$ corresponds to the largest value of p where all the singular values of $\Psi_i^T \Psi_j$ are strictly less than 1. Therefore, the number of positive singular values smaller than one is equal to p if $1 \leq p < n/2$; and $n - p$ if $n/2 \leq p < n$. Thus, one can conclude that when $p = n/2$ the expected value of the off-diagonal entries $\bar{k}_{ij}(p, n)$ of $k_{bc}(\Psi_i, \Psi_j)$ is minimal.

Next, a lemma for the diagonal elements of the Binet-Cauchy kernel matrix k_{bc} is presented.

LEMMA 4.6. *Given two random subspaces $\mathcal{X}_i = \text{span}(\Psi_i)$ and $\mathcal{X}_j = \text{span}(\Psi_j)$ on $\mathcal{G}(p, n)$, if $i = j$ the entries in the diagonal of $k_{bc}(\Psi_i, \Psi_j)$ are given by $k_{ii} = 1$.*

Proof. The proof of lemma 4.6 is trivial because $\cos^2(\theta_i) = 1$ for $i = 1, \dots, p$ in Eq. (4.3). \square

One can start the analysis of the off-diagonal entries of the Binet-Cauchy kernel matrix from the trivial cases. Considering two random subspaces \mathcal{X}_i and \mathcal{X}_j one can easily show that for $p = 1$ the expected value of the off-diagonal entries of the Binet-Cauchy kernel is given by $\bar{k}_{ij}(p, n) = 1/n$, as in the projection kernel. On the other hand, for $p = n$, which is an extreme case used for theoretical purposes only, one can

observe that $k_{ij}(p) = 1$ because all the principal angles are equal to zero. Therefore, in the extreme cases both kernels have similar behavior. More generally, one can show that the expected values of the off-diagonal entries of the Binet-Cauchy kernel can be obtained using the joint probability density function in Eq. (4.9). However, this calculation is cumbersome and an upper bound for the expected value of the off-diagonal entries of the Binet-Cauchy kernel matrix can be defined as presented in the following lemma.

LEMMA 4.7. *Given two random subspaces $\mathcal{X}_i = \text{span}(\Psi_i)$ and $\mathcal{X}_j = \text{span}(\Psi_j)$ on $\mathcal{G}(p, n)$ the expected value $\bar{k}_{ij}(p, n)$ of the off-diagonal entries of $k_{bc}(\Psi_i, \Psi_j)$ has the following upper bound*

$$(4.22) \quad \bar{k}_{ij}(p, n) \leq \begin{cases} \left(\frac{p}{n}\right)^p, & \text{if } 1 \leq p < \frac{n}{2} \\ \left(\frac{n-p}{n}\right)^{n-p}, & \text{if } \frac{n}{2} \leq p < n \end{cases}.$$

Proof. Considering the matrices Ψ_i and Ψ_j , presented in the proof of lemma 4.4, as bases of both subspaces \mathcal{X}_i and \mathcal{X}_j , respectively; and using the inequality of arithmetic and geometric means (AM-GM inequality) [13] one can observe that

$$(4.23) \quad \left(\prod_{i=1}^p \mathbb{E}[\sigma_i^2(\xi)]\right)^{\frac{1}{p}} \leq \frac{1}{p} \sum_{i=1}^p \mathbb{E}[\sigma_i^2(\xi)].$$

From lemma 4.4 one can say that $\mathbb{E}[\sigma_i^2(\xi)]$ with $i = 1, \dots, p$ is equal to p/n . Thus, one can write

$$(4.24) \quad \left(\prod_{i=1}^p \mathbb{E}[\sigma_i^2(\xi)]\right)^{\frac{1}{p}} \leq \frac{p}{n}.$$

Therefore, the expected value of the off-diagonal entries of the Binet-Cauchy kernel has an upper bound given by

$$(4.25) \quad \bar{k}_{ij}(p, n) \leq \left(\frac{p}{n}\right)^p,$$

if $p < n/2$. On the other hand, if $n/2 \leq p < n$ the upper bound is given by

$$(4.26) \quad \bar{k}_{ij}(p) \leq \left(\frac{n-p}{n}\right)^{n-p}.$$

In fact, Eq. (4.26) holds because for $n/2 \leq p < n$ only $n-p$ singular values are in the interval $(0, 1)$ and contribute to the product in the left-hand side of Eq. (4.23). \square

As for the projection kernel, a Monte Carlo simulation is performed to verify the consistency of the upper bound presented in this section. In this regard, 3,000 random matrices Ψ_j are sampled from a Gaussian distribution, as presented in the proof of lemma 4.4, for each value of $p = 1, \dots, 19$, with $n = 20$. Thus, it is shown in Fig. 4 that the result of lemma 4.7 holds.

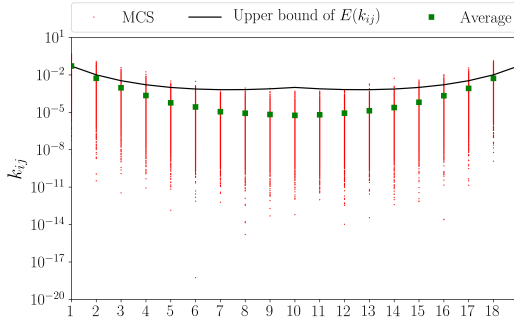


Figure 4: Average from the Monte Carlo simulation and the expected value of the off-diagonal elements of the Binet-Cauchy kernel (in log-scale) as a function of p for $n = 20$.

4.2.3. Kernel dimensionality: comparison. We see from the previous sections that, on average, the elements of the projection kernel grows with order $\mathcal{O}(p^2)$. On the other hand, the elements of the Binet-Cauchy kernel have, on average, a decaying behavior with an upper bound with order $\mathcal{O}(p^p)$ for $1 \leq p < n/2$, and a growing behavior for $n/2 \leq p < n$ with an upper bound with order $\mathcal{O}(p^{n-p})$. This last result is particularly important because the order of the off-diagonal elements of the Binet-Cauchy kernel reduces at a high rate influencing the behavior of the random walk over a dataset projected onto the Grassmann manifold, which is an important ingredient of the technique developed herein.

More specifically, the decaying behavior of the off-diagonal terms of the affinity matrix for the Binet-Cauchy kernel causes the kernel matrix to approach an undesirable identity matrix as p increases up to $n/2$. On the contrary, the off-diagonal terms of projection kernel matrix grow with p^2 producing a random walk that mixes well and is suitable for kernel-based dimension reduction, as we will see in the next chapter. Thus, the Binet-Cauchy kernel is generally used when p is small relative to n while the projection kernel is used for larger manifold dimensions. In the examples shown later, we are using the projection kernel exclusively for this reason.

5. Grassmannian diffusion maps. The similarity among the elements of a dataset is strongly tied to the geometry of the underlying structure connecting them. This characteristic has been exploited by the conventional diffusion maps [12], where the data similarity is associated with the transition probability of a random walk defined over the dataset. Consequently, complex nonlinear structures can be revealed by a set of coordinates embedding the data in a low-dimensional Euclidean space whereas the local characteristics are preserved, which is not possible when linear methods are employed. The conventional diffusion maps defines the similarity in the ambient Euclidean space where only the graphical perception and not the algebraic characteristics of each element in the dataset is taken into consideration. In pattern recognition, for instance, the local geometry of the elements of a dataset is relevant to characterize the underlying mechanism or features responsible for their shapes in the ambient space. Therefore, the theory of Grassmann manifolds can be used in this context where every element in the dataset can be projected onto a Grassmann manifold where similarity is defined by the affinity between the subspaces and where the redundant features can be discarded.

The arguments presented in the previous paragraph serve as motivation for the de-

velopment of a novel dimensionality reduction technique composed of both a pointwise and a multipoint dimensionality reduction. The pointwise dimensionality reduction corresponds to the projection of the high-dimensional elements of a dataset onto a Grassmann manifold encoding their local geometric structure, where points on the Grassmann manifold is an equivalent class defined by a point on the Stiefel manifold. Next, a set of subspaces represented by their respective basis is determined to be used by the multipoint dimensionality reduction step. Thus, a graph is designed connecting the points on the Grassmann manifold with similarity determined by a Grassmannian kernel embedding the Grassmann manifold into a Hilbert space. Therefore, a random walk can be performed over points on the Grassmann manifold such that its transition probability can be used to embed the data in a Euclidean space, called diffusion space herein, where one can take advantage of the Euclidean metric in data-driven applications (e.g., data classification). The technique developed herein, referred to as Grassmannian diffusion maps (GDMs), can outperform the conventional diffusion maps when the intrinsic structure of the elements in the dataset is relevant for a given application, as in object classification and facial recognition, for instance.

In the following, we elaborate the theoretical underpinnings of the GDMs in both a continuous and a discrete setting. This is followed by a brief algorithmic description of the method.

5.1. Continuous embedding on Euclidean space. Given a probability space (Ω, \mathcal{F}, P) , where Ω is the sample space, \mathcal{F} is the σ -algebra of subsets of Ω (events), and P is a probability measure satisfying the Kolmogorov axioms [32], one can define a map $(\Omega, \mathcal{F}, P) \xrightarrow{X} (\mathcal{G}(p, n), \mathcal{A}, V)$, where \mathcal{A} is the σ -algebra formed by the Borel sets on $\mathcal{G}(p, n)$; X is a random variable $X : \Omega \rightarrow \mathcal{G}(p, n)$; and V is a volume measure on $\mathcal{A}(\mathcal{G})$ defined as $dV(\mathcal{X}) = \sqrt{|g_{\mathcal{X}}|} d\mathcal{X}$, where $|g_{\mathcal{X}}|$ is the determinant of the metric tensor $g_{\mathcal{X}}$, and $d\mathcal{X}$ is a Lebesgue measure [4]. Next, let's consider a set of points $S = \{\mathbf{X}_i\}$ in the ambient space, where $\mathbf{X}_i \in \mathbb{R}^{n \times m}$, with projections on the Grassmann manifold $\mathcal{G}(p, n)$ given by $G = \{\mathcal{X}_i\}$, with $i = 1, \dots, N$. Given a positive semi-definite kernel $k : \mathcal{G}(p, n) \times \mathcal{G}(p, n) \rightarrow \mathbb{R}$, a reversible Markov chain can be defined on G where a transition kernel on $\mathcal{G}(p, n)$ can be determined by

$$(5.1) \quad p(\mathcal{X}, \mathcal{Y}) = \frac{k(\mathcal{X}, \mathcal{Y})}{d(\mathcal{X})},$$

with

$$(5.2) \quad \int_G p(\mathcal{X}, \mathcal{Y}) dV(\mathcal{Y}) = 1.$$

Thus,

$$(5.3) \quad d(\mathcal{X}) = \int_G k(\mathcal{X}, \mathcal{Y}) dV(\mathcal{Y}),$$

is a positive function defining the degree of the graph on G . Considering that $p_t(\mathcal{X}, \mathcal{Y})$ corresponds to the t -step transition probability of the random walk on $\mathcal{G}(p, n)$, one can define a diffusion operator on G as

$$(5.4) \quad \mathcal{D}^t f(\mathcal{X}) = \int_G p_t(\mathcal{X}, \mathcal{Y}) f(\mathcal{Y}) dV(\mathcal{Y}),$$

which can be viewed as the one-step transition probability of a stationary Markov chain $W = (G, V, p)$ on $\mathcal{G}(p, n)$. Assuming the stationary distribution of the Markov

chain W over G given by Π , one can obtain the probability density function $\pi(\mathcal{X})$ as

$$(5.5) \quad \pi(\mathcal{X}) = \frac{d(\mathcal{X})}{\int_G d(\mathcal{Y})dV(\mathcal{Y})},$$

As the Markov chain is stationary, one can notice that $\Pi(\mathcal{D}^t f(\mathcal{X})) = \Pi(f(\mathcal{X})) = \int_G f(\mathcal{X})d\Pi(\mathcal{X})$, where f is a bounded measurable function [10]. Moreover, for a reversible Markov chain, which is associated with a symmetric graph, one can get

$$(5.6) \quad \pi(\mathcal{X})p(\mathcal{X}, \mathcal{Y}) = \pi(\mathcal{Y})p(\mathcal{Y}, \mathcal{X}).$$

It is worth mentioning that from Eq. (5.5) it is possible to show that W admits a spectral decomposition [12]. In this regard, conjugating $p(\mathcal{X}, \mathcal{Y})$ by $\sqrt{\pi(\mathcal{Y})}$ one can obtain

$$(5.7) \quad \kappa(\mathcal{X}, \mathcal{Y}) = \frac{k(\mathcal{X}, \mathcal{Y})}{\sqrt{\pi(\mathcal{X})}\sqrt{\pi(\mathcal{Y})}}.$$

Where the spectral decomposition of $\kappa(\mathcal{X}, \mathcal{Y})$ exists when

$$(5.8) \quad \int_G \int_G \kappa^2(\mathcal{X}, \mathcal{Y})dV(\mathcal{X})dV(\mathcal{Y}) < +\infty.$$

Thus, the following eigendecomposition can be obtained [12]

$$(5.9) \quad \kappa(\mathcal{X}, \mathcal{Y}) = \sum_{j=0}^{\infty} \lambda_j \phi_j(\mathcal{X})\phi_j(\mathcal{Y}),$$

Considering that W is aperiodic and the graph is connected, the Markov chain is ergodic; thus, $1 = \lambda_0 > \lambda_1 \geq \dots \geq 0$ (see [12, 10]). Further, ϕ_j is an orthonormal set of eigenfunctions with $\phi_0(\mathcal{X}) = \sqrt{\pi(\mathcal{X})}$. Thus, $p(\mathcal{X}, \mathcal{Y})$ also assumes the following decomposition.

$$(5.10) \quad p(\mathcal{X}, \mathcal{Y}) = \sum_{j=0}^{\infty} \lambda_j \psi_j(\mathcal{X})\tilde{\psi}_j(\mathcal{Y}) = \pi(\mathcal{Y}) + \sum_{j=1}^{\infty} \lambda_j \psi_j(\mathcal{X})\tilde{\psi}_j(\mathcal{Y}),$$

where $\psi_j(\mathcal{X}) = \phi_j(\mathcal{X})/\sqrt{\pi(\mathcal{X})}$ and $\tilde{\psi}_j(\mathcal{Y}) = \phi_j(\mathcal{Y})\sqrt{\pi(\mathcal{Y})}$. Therefore, one can write

$$(5.11) \quad \mathcal{D}\psi_j = \lambda_j \psi_j, \text{ for } j = 1, 2, \dots$$

According to [12] a notion of distance $\delta(\mathcal{X}, \mathcal{Y})$ in the L_2 sense between two transition probabilities at step $t \in \mathbb{N}_+$ can be described based on the graph connectivity, where points highly connected by short paths will have a smaller distance due to the large transition probability of the random walk in moving from one point to the other. Thus, one can write

$$(5.12) \quad \delta(\mathcal{X}, \mathcal{Y}) := \|p_t(\mathcal{X}, \cdot) - p_t(\mathcal{Y}, \cdot)\|_{L_2(dV/\pi)} = \left\{ \int_G [p_t(\mathcal{X}, \mathcal{Z}) - p_t(\mathcal{Y}, \mathcal{Z})]^2 \frac{dV(\mathcal{Z})}{\pi(\mathcal{Z})} \right\}^{\frac{1}{2}}.$$

From Eqs. (5.10-5.12) one can easily see that the diffusion distance $\delta(\mathcal{X}, \mathcal{Y})$ can be defined in terms of the spectral representation of the transition probabilities $p_t(\mathcal{X}, \mathcal{Y})$. Therefore, the following lemma for the spectral representation of the diffusion distance holds.

LEMMA 5.1. *The diffusion distance $\delta(\mathcal{X}, \mathcal{Y})$ admits a spectral representation in the form*

$$(5.13) \quad \delta(\mathcal{X}, \mathcal{Y}) = \left\{ \sum_{j=1}^{\infty} \lambda_j^{2t} [\psi_j(\mathcal{X}) - \psi_j(\mathcal{Y})]^2 \right\}^{\frac{1}{2}}.$$

Proof. Substituting Eq. (5.10) in Eq. (5.12) one can write its square value as

$$(5.14) \quad \delta(\mathcal{X}, \mathcal{Y})^2 = \left\| \sum_{j=0}^{\infty} \lambda_j^t \psi_j(\mathcal{X}) \tilde{\psi}_j(\mathcal{Z}) - \sum_{j=0}^{\infty} \lambda_j^t \psi_j(\mathcal{Y}) \tilde{\psi}_j(\mathcal{Z}) \right\|_{L_2(1/\pi)}^2.$$

Assuming $1/\tilde{\psi}_0(\mathcal{Z})$ as the selected weight, one can easily show that

$$(5.15) \quad \delta(\mathcal{X}, \mathcal{Y})^2 = \sum_{\mathcal{Z} \in G} \left\{ \sum_{j=1}^{\infty} \lambda_j^t [\psi_j(\mathcal{X}) - \psi_j(\mathcal{Y})] \tilde{\psi}_j(\mathcal{Z}) \right\}^2 \frac{1}{\pi(\mathcal{Z})}.$$

However, considering that $\tilde{\psi}_j(\mathcal{Z}) = \phi_j(\mathcal{Z}) \sqrt{\pi(\mathcal{Z})}$, one can show that

$$(5.16) \quad \delta(\mathcal{X}, \mathcal{Y})^2 = \sum_{\mathcal{Z} \in G} \left\{ \sum_{j=1}^{\infty} \lambda_j^t [\psi_j(\mathcal{X}) - \psi_j(\mathcal{Y})] \phi_j(\mathcal{Z}) \right\}^2.$$

As we are considering that ϕ is orthonormal, one can manipulate Eq. (5.16) such that

$$(5.17) \quad \delta(\mathcal{X}, \mathcal{Y})^2 = \sum_{j=1}^{\infty} \lambda_j^{2t} [\psi_j(\mathcal{X}) - \psi_j(\mathcal{Y})]^2,$$

showing that Eq. (5.13) is valid. \square

The result presented in Eq. (5.13) is important for the following lemma describing the relationship between the diffusion distance and the distance metric in the Euclidean space.

LEMMA 5.2. *A set of coordinates given by*

$$(5.18) \quad \Xi_t(\mathcal{X}) = (\xi_0^t(\mathcal{X}), \xi_1^t(\mathcal{X}), \dots) = (\lambda_0^t \psi_0(\mathcal{X}), \lambda_1^t \psi_1(\mathcal{X}), \dots),$$

are known as diffusion maps and embed the points of the Grassmann manifold into a Euclidean space where the Euclidean distance is equal to the diffusion distance.

Proof. One can easily show that the L_2 -norm of $\Xi_t(\mathcal{X}) - \Xi_t(\mathcal{Y})$ is given by

$$(5.19) \quad \|\Xi_t(\mathcal{X}) - \Xi_t(\mathcal{Y})\|_{L_2} = \left\{ \sum_{j=1}^{\infty} \lambda_j^{2t} [\psi_j(\mathcal{X}) - \psi_j(\mathcal{Y})]^2 \right\}^{\frac{1}{2}},$$

thus, $\delta(\mathcal{X}, \mathcal{Y}) = \|\Xi_t(\mathcal{X}) - \Xi_t(\mathcal{Y})\|_{L_2}$, proving lemma 5.2. \square

However, due to the decaying nature of the spectrum $\{\lambda_j^t\}_{t \in \mathbb{N}_+}$, which is also related to the connectivity of the graph, one can truncate the summation in Eq. (5.13) until $j = q$ where $\lambda_j^t \approx 0$ for $j > q$. Thus,

$$(5.20) \quad \delta_q(\mathcal{X}, \mathcal{Y}) \simeq \left\{ \sum_{j=1}^q \lambda_j^{2t} [\psi_j(\mathcal{X}) - \psi_j(\mathcal{Y})]^2 \right\}^{\frac{1}{2}}.$$

5.2. Discrete embedding on Euclidean space. Assuming a set of i.i.d. random samples $S_N = \{\mathbf{X}_1, \dots, \mathbf{X}_N\}$, with probability distribution f and $\mathbf{X}_i = \mathbb{R}^{n \times m}$ for $i = 1, \dots, N$, their projections onto the Grassmann manifold $\mathcal{G}(p, n)$ are given by $G_N = \{\mathcal{X}_1, \dots, \mathcal{X}_N\}$. Next, considering a positive semi-definite kernel $k : \mathcal{G}(p, n) \times \mathcal{G}(p, n) \rightarrow \mathbb{R}$ imposing weights to the edges of a graph where a random walk $W_N = (S_N, f, \mathbf{P})$ is performed, one can construct the transition probability P resorting to the graph Laplacian normalization. In this regard, the discrete counterpart of the degree function presented in Eq. (5.3) is given by the following diagonal matrix $\mathbf{D} \in \mathbb{R}^{N \times N}$

$$(5.21) \quad D_{ii} = \sum_{j=1}^N k(\mathcal{X}_i, \mathcal{X}_j),$$

where the stationary distribution of the random walk is given by

$$(5.22) \quad \pi_i = \frac{D_{ii}}{\sum_{k=1}^N D_{kk}},$$

corresponding to the discrete counterpart of Eq. (5.5). Next, the spectral decomposition of the random walk W_N is presented. First, the kernel matrix $k_{ij} = k(\mathcal{X}_i, \mathcal{X}_j)$ is normalized as follows

$$(5.23) \quad \kappa_{ij} = \frac{k_{ij}}{\sqrt{D_{ii}D_{jj}}},$$

which is equivalent to Eq. (5.7), where the transition probability P_{ij} of the random walk W_N over G_N is constructed as

$$(5.24) \quad P_{ij}^t = \frac{\kappa_{ij}}{\sum_{k=1}^N \kappa_{ik}}.$$

From the eigendecomposition of \mathbf{P}^t , one can obtain the first q eigenvectors $\{\psi_k\}_{k=0}^q$, where $\psi_k \in \mathbb{R}^N$ and their respective eigenvalues $\{\lambda_k\}_{k=0}^q$. In this regard, the diffusion coordinates for the element i in the dataset is given by

$$(5.25) \quad \Xi_j = (\xi_{j0}, \dots, \xi_{jq}) = (\lambda_0 \psi_{j0}, \dots, \lambda_1 \psi_{jq}),$$

where ψ_{jk} corresponds to the position j of ψ_k . Next, definition of the diffusion distance for the discrete embedding of the Grassmann manifold in the Euclidean space uses lemma 5.1, such that

$$(5.26) \quad \delta_{ij} = \|p_{ik}^t - p_{jk}^t\|_{L_2(D_{ii}^{-1})} = \left\{ \sum_{k=1}^N [p_{ik}^t - p_{jk}^t]^2 \frac{1}{D_{kk}} \right\}^{\frac{1}{2}},$$

whose spectral representation is given by

$$(5.27) \quad \delta_{ij} = \left\{ \sum_{k=1}^N \lambda_k^{2t} [\psi_{ik} - \psi_{jk}]^2 \right\}^{\frac{1}{2}}.$$

Next, an algorithm summarizing the main steps used in the Grassmannian diffusion maps is presented.

Algorithm 5.1 Grassmannian Diffusion Maps (GDM)

Require: a set of N high-dimensional data $S_N = \{\mathbf{X}_1, \dots, \mathbf{X}_N\}$ with $\mathbf{X}_i \in \mathbb{R}^{n \times m}$, and the dimension p of the Grassmann manifold.

- 1: **for** $i \in 1, \dots, N$ **do**
- 2: Compute the thin Singular Value Decomposition: $\mathbf{X}_i = \Psi_i \Sigma_i \Phi_i^T$, where $\Psi_i \in \mathcal{G}(p, n)$ and $\Phi_i \in \mathcal{G}(p, m)$.
- 3: **end for**
- 4: For every pair $[\Psi_i, \Psi_j]$ and $[\Phi_i, \Phi_j]$ compute the entries of k_{ij} of the kernel matrices $k_{ij}(\Psi)$ and $k_{ij}(\Phi)$, either using Eq. (4.2) or Eq. (4.4).
- 5: Compute the composed kernel matrix $k(\Psi, \Phi)$. For example:

$k(\Psi, \Phi) = k_{ij}(\Psi) + k_{ij}(\Phi)$ or $k(\Psi, \Phi) = k_{ij}(\Psi) \circ k_{ij}(\Phi)$, where \circ is the Hadamard product.
- 6: Compute diagonal matrix $\mathbf{D} \in \mathbb{R}^{N \times N}$ using $k(\Psi, \Phi)$ in Eq. (5.21).
- 7: Compute the normalized kernel matrices using Eq. (5.23) for $k(\Psi, \Phi)$.
- 8: Estimate the transition matrix \mathbf{P}^t of the Markov chain over the data on the Grassmann manifold.
- 9: Obtain the eigenvectors and their respective eigenvalues from the eigendecomposition of \mathbf{P}^t and determine the truncation index q .

Ensure: diffusion coordinates Ξ_1, \dots, Ξ_N , with $\Xi_i \in \mathbb{R}^q$.

6. Grassmannian diffusion maps based data classification. Several techniques, such as Eigenfaces [52], Fisherfaces [7], and Laplacianfaces [29], seek to project high-dimensional data (e.g., face images) onto a low-dimensional feature space where the classification/recognition can be efficiently performed. However, no consensus has been established on which technique is the most appropriate to handle a large amount of data as observed in real-life application. Thus, as a contribution to this effort a data classification/recognition technique based on sparse representation is developed herein taking advantage of the ability of the Grassmannian diffusion maps in discarding redundant information present in high-dimension data. Among the advantages of this approach one can mention its capability to perform the classification/recognition based on a low-dimensional dictionary and its robustness.

The theory of compressed sensing and sparse representation have been employed in several application, such as in spectral identification [33, 16, 34], robust PCA [9], matrix completion [41], missing pixel recovery [49], and robust face recognition [59]. In particular, compressed sensing seeks to compute a linear representation of a model with respect to an overcomplete dictionary of bases elements (e.g., wavelets and Fourier basis), where a sparse representation can be obtained solving a convex optimization problem in the l_0 -norm sense; however, this problem is NP-hard resulting in a combinatorial problem. On the other hand, solving it in the l_2 -norm sense could not yield a sparse solution. To circumvent such limitations, the optimization problem can be relaxed to be solved in the l_1 -norm sense. However, the compressed sensing technique is not typically employed in classification problems and a more appropriate approach considering an overcomplete dictionary of the diffusion coordinates is developed herein. This novel method takes advantage of the ability of the sparse representation-based classification method [59] in determining a linear and compact combination of the elements in the dictionary to represent a testing data with the advantage that the intrinsic geometric structure of the data is explicitly considered

when the Grassmann manifold is mapped into a Euclidean space. Moreover, the amount of stored data is a fraction of the necessary to create a proper dictionary in the conventional approach.

Let's first assume a training set $T_N = \{\mathbf{X}_i\}_{i=1}^N$ with $\mathbf{X}_i \in \mathbb{R}^{n \times m}$, and k distinct classes. Using the Grassmannian diffusion maps, as presented in the previous section, over the augmented dataset $T_{N+1} = \{\mathbf{X}_1, \dots, \mathbf{X}_N, \mathbf{X}_T\}$, where \mathbf{X}_T is the test sample, one can obtain the diffusion coordinates of each element in T_{N+1} assuming that each element lies on the same Grassmann manifold $\mathcal{G}(p, n)$. Therefore, the diffusion coordinates of each element in the k -th class are arranged as the columns of a matrix $\mathbf{A}_k \doteq [\mathbf{\Xi}_{k,1}, \dots, \mathbf{\Xi}_{k,N_k}] \in \mathbb{R}^{q \times N_k}$, where N_k is the number of elements in class k , and q is the truncation index used to define the dimension of the diffusion space. This approach assumes that any test sample given by its diffusion coordinates $\mathbf{\Xi}_T$ will lie in the linear span of the training samples in a given class which is given by

$$(6.1) \quad \mathbf{\Xi}_T = c_{k,1}\mathbf{\Xi}_{k,1} + \dots + c_{k,N_k}\mathbf{\Xi}_{k,N_k},$$

where $c_{k,j} \in \mathbb{R}$ with $j = 1, \dots, N_k$. Therefore, the dictionary \mathbf{A} can be constructed concatenating k matrices \mathbf{A}_k , such as

$$(6.2) \quad \mathbf{A} \doteq [\mathbf{A}_1, \dots, \mathbf{A}_{N_k}] \in \mathbb{R}^{q \times N}.$$

Therefore, the following underdetermined ($N > q$) linear systems is obtained.

$$(6.3) \quad \mathbf{\Xi}_T = \mathbf{A}\mathbf{c},$$

where the constant vector $\mathbf{c} = [0, \dots, 0, c_{k,1}, \dots, c_{k,N_k}, 0, \dots, 0]^T \in \mathbb{R}^N$ has non-zero value in the entries associated to the k -th class. It is evident that the solution of an underdetermined system is not unique; however, the sparsest solution of the system in Eq. (6.3) can be found solving a convex optimization problem in the l_0 -norm sense, expressed by

$$(6.4) \quad \hat{\mathbf{c}} = \operatorname{argmin} \|\mathbf{c}\|_0 \quad \text{subject to} \quad \mathbf{A}\mathbf{c} = \mathbf{\Xi}_T.$$

However, this problem is NP-hard and finding a solution depends on the solution of a combinatorial problem on \mathbf{c} . On the other hand, a solution in the l_2 -norm sense will not provide any useful information because it yields a dense vector $\hat{\mathbf{c}}$. Therefore, a relaxation of the necessary conditions to obtain the exact solution with high probability is necessary and the optimization problem can be solved in the l_1 -norm sense. For instance, if $\hat{\mathbf{c}}$ is sufficiently sparse, the exact solution can be recovered with high probability [59]. Moreover, it is natural that real-life data be corrupted with some level of noise; thus, it is necessary to take this possibility into consideration such that an approximation of the solution of the linear system in Eq. (6.3) is sought instead of the exact solution. In this regard, the optimization problem to be solved is given by

$$(6.5) \quad \hat{\mathbf{c}} = \operatorname{arg min} \|\mathbf{c}\|_1 \quad \text{subject to} \quad \|\mathbf{A}\mathbf{c} - \mathbf{\Xi}_T\|_2^2 \leq \epsilon,$$

or by its unconstrained form,

$$(6.6) \quad \hat{\mathbf{c}} = \operatorname{arg min} \|\mathbf{A}\mathbf{c} - \mathbf{\Xi}_T\|_2^2 + \beta \|\mathbf{c}\|_1,$$

where ϵ is the error tolerance and β is the regularization constant. Next, once the vector of coefficients $\hat{\mathbf{c}}$ is determined, one can perform the classification either by

assigning the maximum entry of $\hat{\mathbf{c}}$ to its associated class or by identifying the class yielding the smallest error in the approximation. Clearly, different methods can be employed when performing this task; however, in the last case one can use the information of the subspace structure in the diffusion space. In this regard, a residual can be computed as

$$(6.7) \quad r(k) = \|\mathbf{A}(\mathbf{I}_k^* \circ \hat{\mathbf{c}}_k) - \Xi_T\|_2.$$

Therefore, the classification is performed finding k minimizing $r(k)$, where $\mathbf{I}_k^* \in \mathbb{R}^q$ is a vector whose elements associated to the k -th class are equal to one and the rest are zero, and \circ is the Hadamard product. Next, an algorithm summarizing the steps used in this classification approach is presented.

Algorithm 6.1 GDM based data classification using sparse representation

Require: a set of N high-dimensional data $T_N = \{\mathbf{X}_1, \dots, \mathbf{X}_N\}$ with $\mathbf{X}_i \in \mathbb{R}^{n \times m}$, the dimension p of the Grassmann manifold, and a test sample $\mathbf{X}_T \in \mathbb{R}^{n \times m}$.

- 1: **for** $i \in 1, \dots, N$ **do**
- 2: Compute the thin Singular Value Decomposition: $\mathbf{X}_i = \Psi_i \Sigma_i \Phi_i^T$; where, $\Psi_i \in \mathcal{G}(p, n)$ and $\Phi_i \in \mathcal{G}(p, m)$.
- 3: **end for**
- 4: Compute the thin Singular Value Decomposition: $\mathbf{X}_T = \Psi_T \Sigma_T \Phi_T^T$; where, $\Psi_T \in \mathcal{G}(p, n)$ and $\Phi_T \in \mathcal{G}(p, m)$.
- 5: For the augmented sets $\Psi = \{\Psi_1, \dots, \Psi_N, \Psi_T\}$ and $\Phi = \{\Phi_1, \dots, \Phi_N, \Phi_T\}$ compute the entries of k_{ij} of the kernel matrices $k_{ij}(\Psi)$ and $k_{ij}(\Phi)$ using either Eq. (4.2) or Eq. (4.4).
- 6: Compute the composed kernel matrix $k(\Psi, \Phi)$. For example:
 $k(\Psi, \Phi) = k_{ij}(\Psi) + k_{ij}(\Phi)$ or $k(\Psi, \Phi) = k_{ij}(\Psi) \circ k_{ij}(\Phi)$, where \circ is the Hadamard product.
- 7: Compute the diffusion coordinates $\Xi_1, \dots, \Xi_N, \Xi_T$ as in Algorithm 5.1, with $\Xi_i \in \mathbb{R}^q$.
- 8: Concatenate the Ξ_i 's of each class k as columns of a matrix $\mathbf{A}_k \in \mathbb{R}^{q \times N_k}$.
- 9: Create the matrix of training diffusion coordinates $\mathbf{A} = [\mathbf{A}_1, \dots, \mathbf{A}_{N_k}] \in \mathbb{R}^{q \times N}$.
- 10: Normalize the columns of \mathbf{A} and the test sample Ξ_T to have unit l_2 -norm.
- 11: Solve the convex optimization problem:

$$\hat{\mathbf{c}} = \arg \min \|\mathbf{c}\|_1 \quad \text{subject to} \quad \|\mathbf{A}\mathbf{c} - \Xi_T\|_2^2 \leq \epsilon$$

or alternatively

$$\hat{\mathbf{c}} = \arg \min \|\mathbf{A}\mathbf{c} - \Xi_T\|_2^2 + \beta \|\mathbf{c}\|_1$$

- 12: Compute the residuals for each class k : $r(k) = \|\mathbf{A}(\mathbf{I}_k^* \circ \hat{\mathbf{c}}_k) - \Xi_T\|_2$

Ensure: $k(\mathbf{X}_T) = \arg \min_k r(k)$

7. Examples. In this section, three problems are considered to analyze the performance of the Grassmannian diffusion maps in revealing the intrinsic geometric structure of data and performing classification. This dimensionality reduction approach is addressed in both theoretical and practical aspects aiming at the identification of potential applications in different fields. The analysis adopted in all

examples consists in a direct comparison of both the Grassmannian and the conventional diffusion maps techniques. In particular, the Grassmannian diffusion maps employs the projection kernel (Eq. (4.4)) because it is not as sensitive as the Binet-Cauchy kernel to the change in the dimensionality of the Grassmann manifold, as demonstrated in section 4.2. Moreover, in the ensuing analysis the “first” diffusion coordinate corresponds to the one associated to the eigenvalue λ_1 of the transition matrix of the Markov chain. The same reasoning is employed to the following diffusion coordinates successively until the truncation index q . The algorithms of both the conventional and the Grassmannian diffusion maps, were implemented in the UQpy software [43](Uncertainty Quantification with python: <https://uqpyproject.readthedocs.io/en/latest/>), a general purpose Python toolbox for modeling uncertainty in physical and mathematical systems.

7.1. Structured data on the unit sphere in \mathbb{R}^3 . Consider a collection $S_N = \{\mathbf{X}_i\}_{i=1}^N$ of $N = 10,000$ points defining two cone-like structures in \mathbb{R}^3 as presented in Fig. 5a. In this problem, every point in the set S_N is composed of three coordinates (x_1, x_2, x_3) and lie on a surface whose functional form is due to the constraint $\sin(\phi) = \cos^2(\theta)$, in spherical coordinates. Therefore, if the radius r is uniformly distributed in the interval $[0, 2]$ a set of random points can be obtained as shown in Fig. 5 where the colors are defined by the magnitude $\sqrt{x_1^2 + x_2^2 + x_3^2}$. Here we show that using the Grassmannian diffusion maps a well-defined structured parametrization of the points on the Grassmann manifold $\mathcal{G}(1, 3)$, represented by the subspaces spanned by $\Psi \in \mathcal{V}(1, 3)$, is obtained.

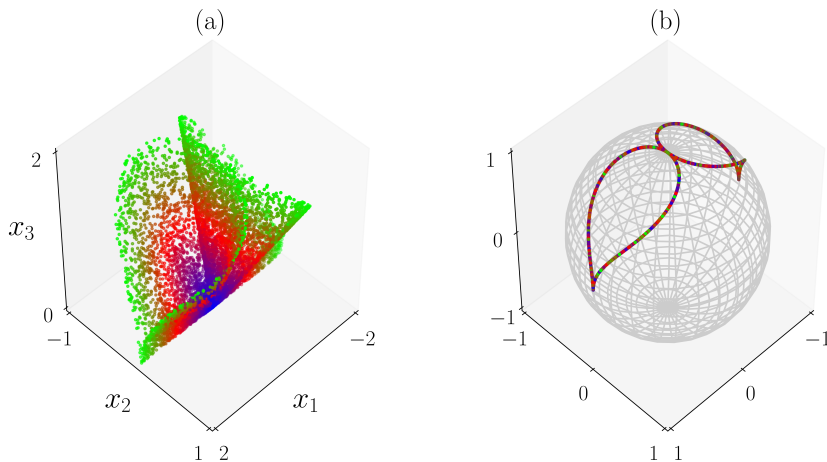


Figure 5: Example 1: (a) Elements of S_N in \mathbb{R}^3 and colored by their magnitude. (b) Projection onto the Grassmann manifold colored by their magnitude in the ambient space.

In the conventional diffusion maps a graph is constructed in the ambient space \mathbb{R}^3 (Fig. 5a), where a Gaussian kernel is used to quantify the similarity between data points. On the other hand, in a Grassmannian perspective the choice of a particular kernel on $\mathcal{G}(1, n)$ is not relevant since both the projection and the Binet-Cauchy kernels will generate the same kernel matrix. In this example, a point on the

Grassmann manifold $\mathcal{G}(1, 3)$ corresponds to a subspace of \mathbb{R}^3 represented by its basis, which is given by a unit vector of \mathbb{R}^3 . Therefore, the collection of the unit vectors in \mathbb{R}^3 representing the set of subspaces of \mathbb{R}^3 is simply represented by the unit sphere in \mathbb{R}^3 . Thus, the points in the ambient space \mathbb{R}^3 have a representation on $\mathcal{G}(1, 3)$ given by the unit vectors in \mathbb{R}^3 (Fig. 5b). In this regard, the notion of distance and affinity are established via the geodesics connecting the points given by the intersection of the unit vector and the unit sphere, and the angle between the unit vectors, respectively.

Herein, we are interested in computing a Grassmannian kernel defining the affinity between pairs of subspaces; thus, once the points are projected onto $\mathcal{G}(1, 3)$, a Grassmannian kernel matrix is employed in the determination of the diffusion coordinates. Once the eigendecomposition of the transition matrix is performed, the eigenvalues can be used to investigate the dimensionality of the embedded structure. In this regard, Fig. 6 shows the decaying behavior of the eigenvalues of the transition probability matrix defined in Eq. (5.24).

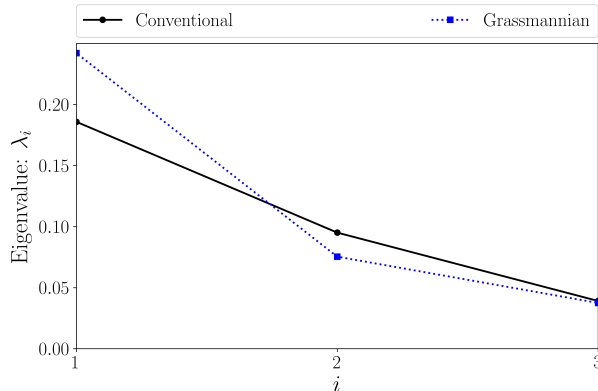


Figure 6: Eigenvalues of the transition matrix for both the conventional and Grassmannian diffusion maps.

Next, the first two diffusion coordinates as points in \mathbb{R}^2 for both the conventional and the Grassmannian diffusion maps are presented in Fig. 7. In particular, Figs. 7a and 7b show the diffusion coordinates for the conventional diffusion maps with a color map defined by the first and the second diffusion coordinates, respectively. On the other hand, Fig. 7c and 7d show the diffusion coordinates for the Grassmannian diffusion maps with a color map defined by the first and the second diffusion coordinates, respectively. One can easily see that the Grassmannian diffusion maps reveals a well-defined unidimensional geometric structure connecting the data points, whereas the conventional diffusion maps reveals a higher-dimensional (bidimensional) structure connecting the elements of the dataset.

The effect of the dimensionality of the embedded structure is observed when the data points are mapped in both the ambient space \mathbb{R}^3 and on the Grassmann manifold $\mathcal{G}(1, 3)$ using the color maps defined by the first and the second diffusion coordinates, for both the conventional (Fig. 8) and the Grassmannian (Fig. 9) diffusion maps. One can easily show that for the conventional diffusion maps both the first and the second diffusion coordinates are mapped in the ambient space \mathbb{R}^3 perpendicularly to the canonical directions, as observed in Figs 8a,c. However, when the same diffusion coordinates are mapped on the Grassmann manifold $\mathcal{G}(1, 3)$ they appear shuffled and no logical parametrization can be extracted from it, as observed in Figs 8b,d. On the

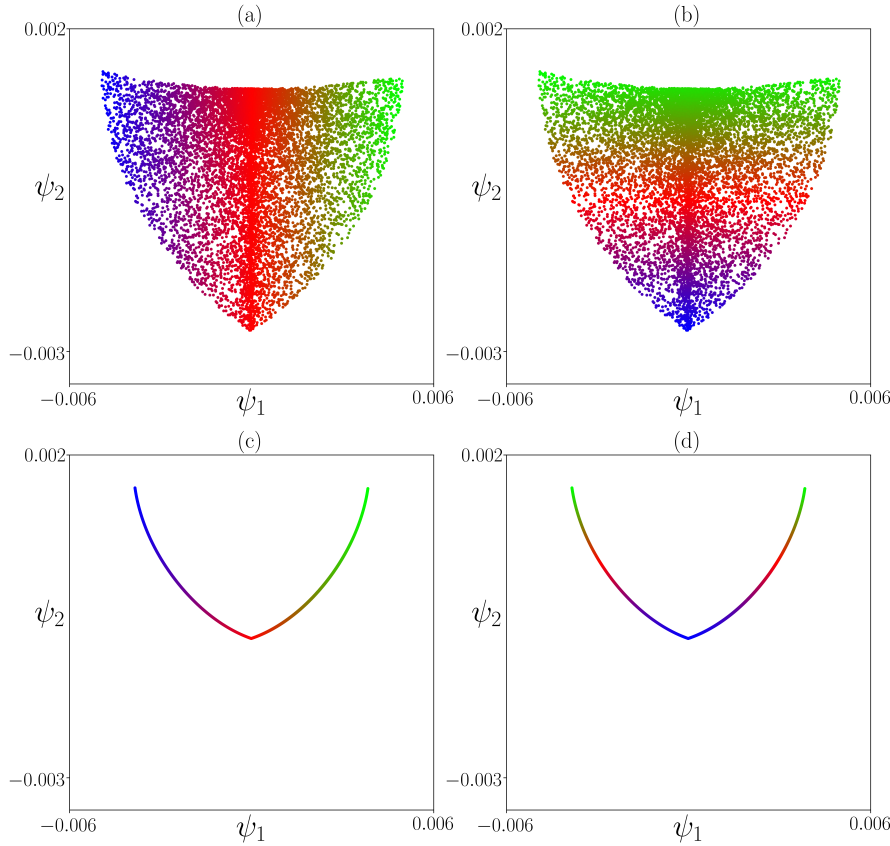


Figure 7: Diffusion coordinates: a) conventional with color map defined by ψ_1 and ψ_2 , b) ψ_2 , c) Grassmannian with color map defined by ψ_1 and by d) ψ_2 .

other hand, for the Grassmannian diffusion maps, the first and the second diffusion coordinates in the ambient space \mathbb{R}^3 (Figs. 9a,c) and on the Grassmann manifold $\mathcal{G}(1, 3)$ (Figs. 9b,d) are clearly structured to align with the intrinsic structure of the data on $\mathcal{G}(1, 3)$.

The results presented in this example gives us a better notion of the ability of the Grassmannian diffusion maps to extract and identify intrinsic data structures. Next, we consider an example using high dimensional data.

7.2. Robust classification of high-dimensional random field data. In this example, the performance of the Grassmannian diffusion maps in revealing the intrinsic geometric structure of high-dimensional data is investigated. Moreover, we explore the GDMs on this data set for the classification of uncertain data performed by applying k-means [36] on the diffusion coordinates aiming at identifying the most important features affecting the shape of the data in the ambient space.

In this regard, the elements of a dataset $S_N = \{\mathbf{X}_1, \dots, \mathbf{X}_N\}$, with $N = 3,000$, are generated with a prescribed rank $p = 5$, where $\mathbf{X}_k \in \mathbb{R}^{n \times m}$ with $n = m = 40$.

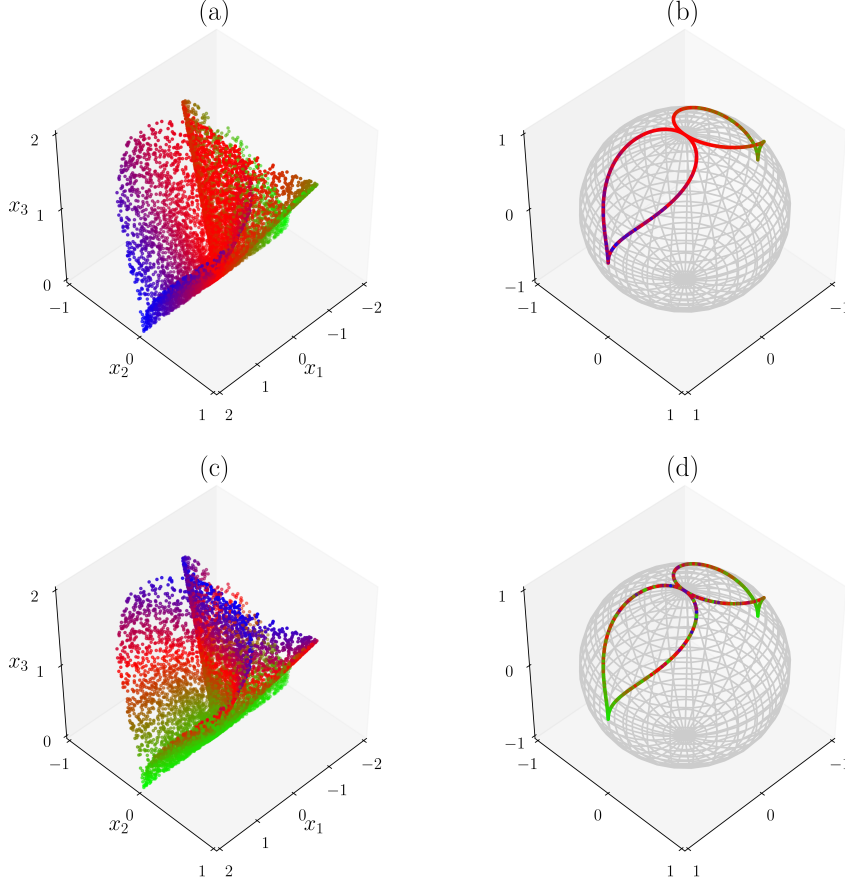


Figure 8: Conventional diffusion maps: color map for ψ_1 in the ambient space a) and on the Grassmann manifold b), and color map for ψ_2 in the ambient space c) and on the Grassmann manifold d).

Thus, each element in the dataset is composed by the following product of matrices

$$(7.1) \quad \mathbf{X}_k = \mathbf{U}_k \mathbf{A}_k \mathbf{U}_k^T,$$

where $\mathbf{A}_k \in \mathbb{R}^{p \times p}$ is a diagonal matrix whose the elements are i.i.d. random numbers with uniform distribution in the interval $(0, 1]$, and the columns of $\mathbf{U}_k \in \mathbb{R}^{n \times p}$ are defined by the following functional form

$$(7.2) \quad u_{ij}^{(k)} = \sqrt{\frac{2}{n}} \cos \left[\frac{2\pi(j + L_k)}{n} (i - T_k) \right],$$

with $j = 0, \dots, p$, and $i = 0, \dots, n - 1$. Moreover, T_k is a discrete random variable assuming integer values in the interval $[0, n - 1]$ with uniform probability, and it represents the phase of the cosine in Eq. (7.2). L_k is also a discrete random variable in the interval $[1, \lfloor \frac{n}{2} \rfloor + 1 - p]$ with uniform probability, which is utilized to define the frequencies of the group of p oscillating functions in the columns of \mathbf{U} . It is worth mentioning

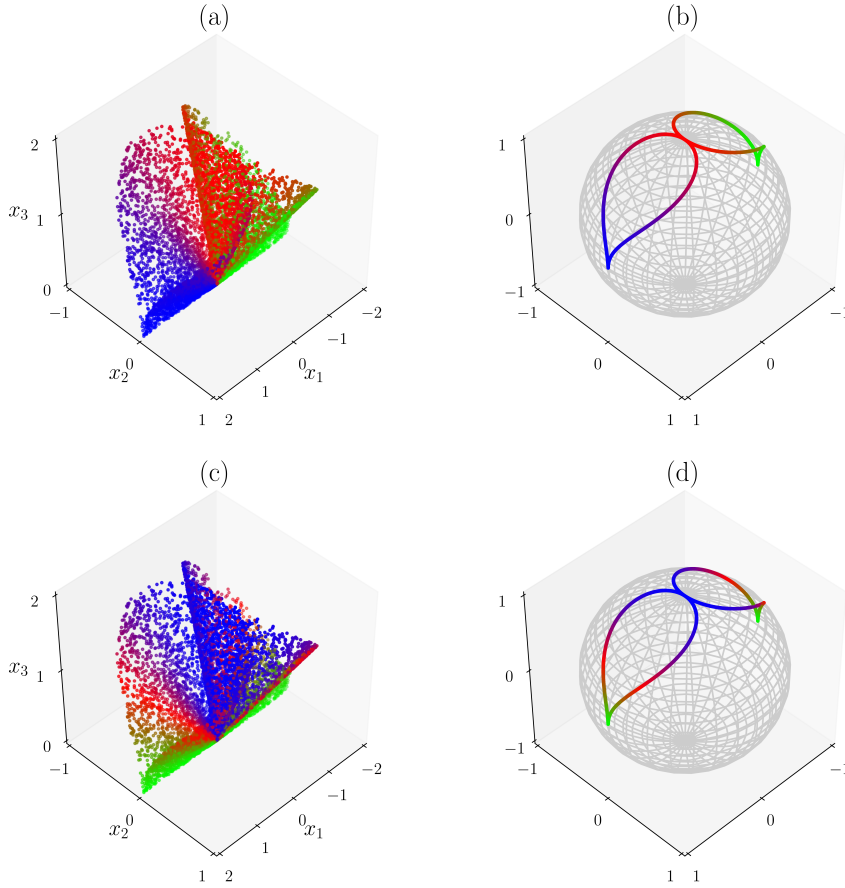


Figure 9: Grassmannian diffusion maps: color map for ψ_1 in the ambient space a) and on the Grassmann manifold b), and color map for ψ_2 in the ambient space c) and on the Grassmann manifold d).

that the samples T_k and L_k are the same for every column of \mathbf{U}_k , meaning that their randomness is associated with the realization of the elements in S_N ; i.e. each element of S_N is a realization of a two-dimensional random field having a stochastic basis. Fig. 10 shows two realizations of \mathbf{X} where $\mathbf{A}_1 = \text{diag}(0.444, 0.828, 0.775, 0.913, 0.981)$, $L_1 = 20$, and $T_1 = 3$; and $\mathbf{A}_2 = \text{diag}(0.614, 0.800, 0.184, 0.519, 0.961)$, $L_2 = 38$, and $T_2 = 6$.

Applying the conventional and Grassmannian diffusion maps to all points in the set S_N , one obtains the eigenvalues of the transition matrix of the Markov chain defined over the dataset, whose decaying behavior is shown in Fig. 11 for both the conventional and the Grassmannian diffusion maps. This decaying behavior shows the embedding capacity of each technique individually, but it does not serve as a comparison tool.

The performance of both techniques are compared by their capacity in revealing the underlying geometry of the random field elements in the set S_N . In this regard,

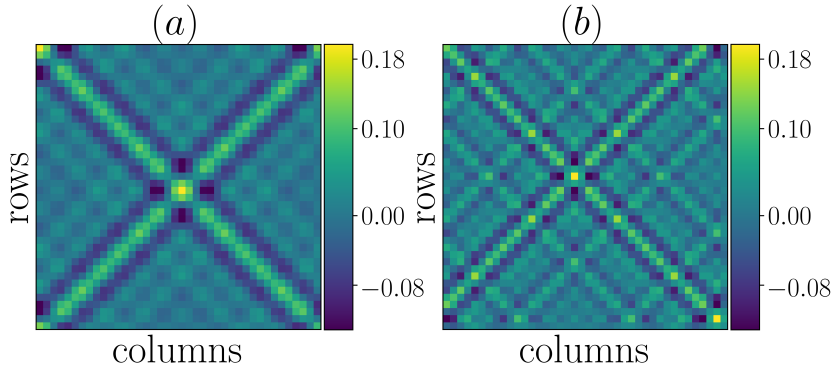
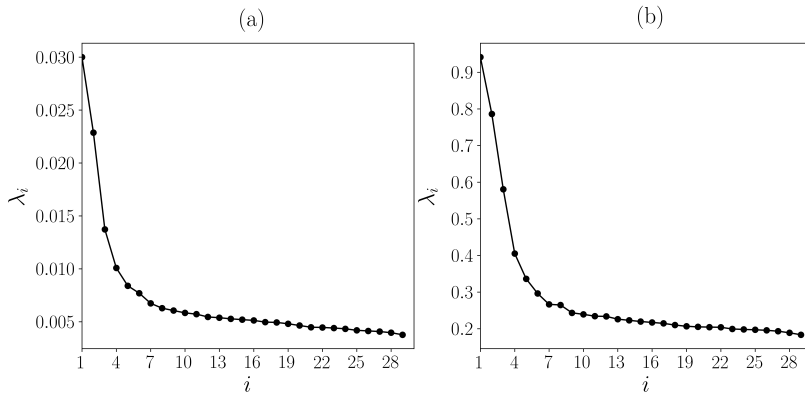
Figure 10: Two realizations of random field elements in S_N .

Figure 11: Eigenvalues of the transition matrix: a) conventional and b) Grassmannian diffusion maps.

a clustering is performed via k-means [36] on the diffusion coordinates such that the most informative features of the random field elements in the dataset are identified. Based on Eq. 6.2 one can argue that the frequency defined by $2\pi(j + L_k)i/n$ should characterize the different subspaces in the Grassmann manifold $\mathcal{G}(5, 40)$, which is not the case for the phase $2\pi(j + L_k)T_k/n$. Therefore, one expects that L_k will have a strong influence on the shape of the points projected onto the Grassmann manifold $\mathcal{G}(5, 40)$. To explore this, the first three diffusion coordinates obtained using the conventional and the Grassmannian diffusion maps are presented in Fig. 12 and in Fig. 13, respectively; where every point defined by the diffusion coordinates corresponds to an element in S_N . Moreover, as 15 values of L_k are considered, we adopt 15 clusters for the k-means algorithm used in the clustering of the diffusion coordinates. When k-means is applied in the diffusion coordinates obtained from the conventional diffusion maps one can observe that the dispersion of the diffusion coordinates adversely influences the clustering, as observed in Fig. (12). This is better observed when the clusters are mapped back to the feature space $(T_k \times L_k)$ in Fig. 14a, where the shuffled colors are an indication that the classification is only based on the information obtained in the ambient space and no intrinsic characteristics of the elements of the

set S_N are considered. On the other hand, Fig. (13) shows that the Grassmannian diffusion maps succeed in identifying the intrinsic geometry of the elements in S_N , where clusters of the Grassmannian diffusion coordinates are clearly delineated. This behavior is evident in Fig. 14b, where the clustering technique is able to identify the elements belonging to the subsets defined by each L_k with $k = 1, \dots, 15$.

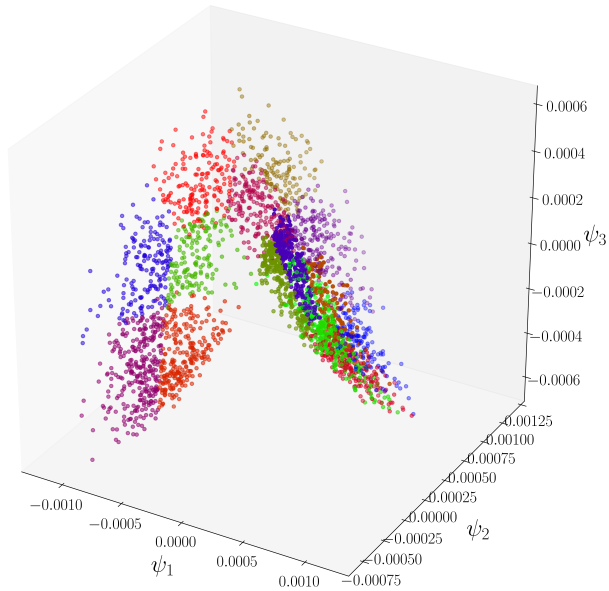


Figure 12: Conventional diffusion maps: k-means applied on the first three diffusion coordinates (15 clusters).

From the results presented in this example it is clear that the Grassmannian diffusion maps has the capability to embed high-dimensional stochastic data in a low-dimensional space taking into consideration their intrinsic local and global geometric structure. This is in contrast to the conventional diffusion maps, where the information provided in the ambient space alone is employed in the determination of a random walk over the data.

7.3. Sparse representation-based facial recognition. In this example, we consider the problem of identifying faces of different subjects considering variation in the illumination, changes in facial expressions, and occurrence of occlusions. To this aim, a sparse representation approach is employed considering a dictionary composed by the diffusion coordinates as presented in section 6. The face images used in this experiment were retrieved from the AT&T Database of Faces (AT&T Laboratories Cambridge). This database contains a set of 400 face images of 40 subjects, corresponding to 10 face images for each subject taken at different times with variation in the illumination, facial expressions (i.e., open and closed eyes, smiling and not smiling faces), and occlusions (i.e., glasses). Moreover, they were taken against a dark and homogeneous background, the subjects had some limited freedom for some side movement, all images are in grey scale and were resized to the dimension 200×200 .

A comparison of the performance of both the conventional and the Grassmannian diffusion maps in identifying the class to which a test subject belongs is presented.

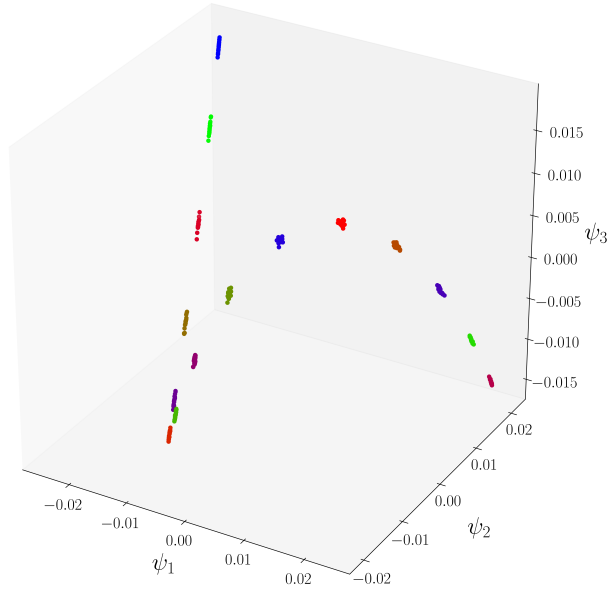


Figure 13: Grassmannian diffusion maps: k-means applied on the first three diffusion coordinates (15 clusters).

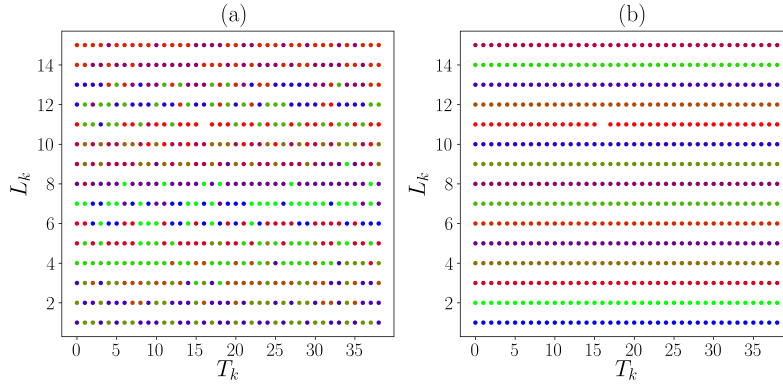


Figure 14: Clusters of the diffusion coordinates mapped in the parameter space ($T_k \times L_k$) (a) Conventional diffusion maps (b) Grassmannian diffusion maps.

In particular, the method presented in Algorithm 6.1 is used in the analysis of the Grassmannian diffusion maps, whereas a modified version is used to include the conventional diffusion maps. This modified algorithm consists in substituting steps 1-6 in Algorithm 6.1 by the conventional diffusion maps using the Gaussian kernel in the elements of S_N , and no value of p is required as an input argument.

Let us assume we have 40 different classes corresponding to a set of 9 face images of the same subject. On the other hand, let's use one single image of each of the 40 subjects as test samples. Therefore, the training set is composed by 360 face images

(40 classes with 9 face images of the same subject each), and the test set composed by 40 face images of distinct subjects. In Fig. (15) each class is represented by one face image of the corresponding subject.



Figure 15: One face image of the subject representing each of 40 classes.

Next, let's consider that a test image is given by the image presented in Fig. (16). The first three diffusion coordinates obtained using conventional diffusion maps on



Figure 16: Test face image.

the augmented set S_N (including the test image) are presented in Fig. (17), whereas the first three diffusion coordinates obtained using the Grassmannian diffusion maps are presented in Fig. (18), with the images projected onto the Grassmann manifold $\mathcal{G}(4, 200)$. In this example, the dimension of the diffusion coordinates is truncated to $q = 20$. Therefore, only 19 dimensions are used in the analysis presented next because dimension 0 corresponds to a constant value for the diffusion coordinate. Although, three dimension are not enough to make a proper qualitative analysis (i.e. we cannot visually see clusters in the three diffusion coordinates), one can observe that the magnitude of the pixels, as observed in the ambient space, is more relevant for the conventional than for the Grassmannian diffusion maps. That is, in the conventional diffusion maps, darker images clearly appear in the top left. Moreover, the condition number of the transition matrix of the Markov process obtained from the conventional diffusion maps is 849 times larger than the one observed in the Grassmannian diffusion maps, which makes the method using the Grassmannian diffusion maps more stable than its conventional counterpart.

Next, we use the diffusion coordinates $\Xi_1, \dots, \Xi_N, \Xi_t$, with $N = 360$, to create the matrix of training coordinates $\mathbf{A} = [\Xi_1 \dots \Xi_N] \in \mathbb{R}^{19 \times 360}$. Moreover, the diffusion coordinates of the training set are given by $\Xi_T \in \mathbb{R}^{19}$. It is worth mentioning that the dimension of the matrix of the training coordinates and the dimension of

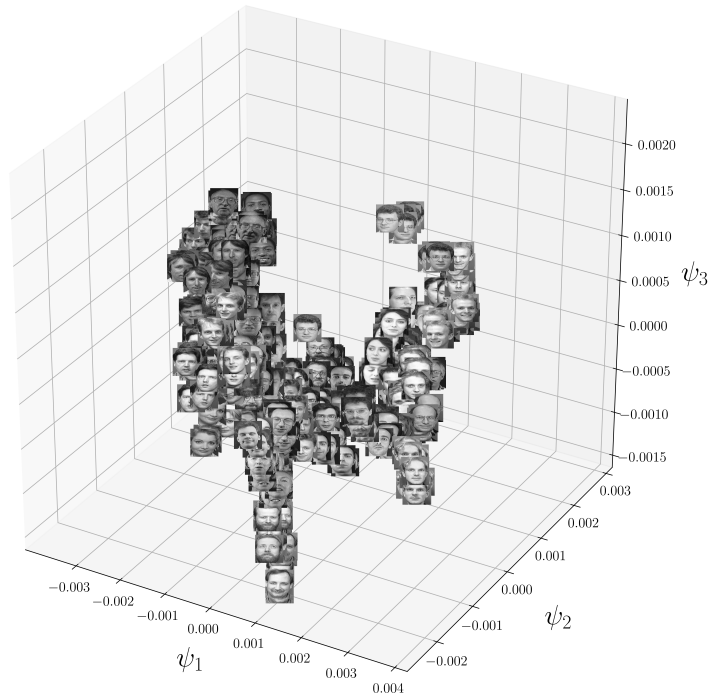


Figure 17: Conventional diffusion maps: face images in the training set plus the test face image in the space defined by the first three diffusion coordinates.

the test sample are much smaller than the dimension of the matrices employed in the conventional sparse representation approach in [59] where the dimension of the matrix of training samples would be $40,000 \times 360$, without downsampling the images, or 100×360 when downsampling each image to size 10×10 . Thus, using both Algorithm 6.1 and its modified version for the conventional diffusion maps we can find the approximate solution $\hat{\mathbf{c}}$ of the following linear system

$$(7.3) \quad \mathbf{\Xi}_T = \mathbf{A}\mathbf{c},$$

either by solving the l_1 -minimization problem in its constrained form (Eq. (6.5) with $\epsilon = 0.1$) or unconstrained form (Eq. (6.6) with $\beta = 1$).

Considering the conventional diffusion maps, we show in Fig. 19a and Fig. 19b the approximated entries of \mathbf{c} as the solutions of both, constrained and unconstrained, minimization problems, respectively. As presented in Fig. 20b and Fig. 20c for both minimization problems, the identified subjects belong to a different class than the test subject, also presented in Fig. 20a. Further, considering the approximation of \mathbf{c} shown in Fig. 19a,b, one can compute the residuals for each class k of subjects using Eq. (6.7) to identify the class k that minimizes $r(k)$. The results for the conventional diffusion maps are presented in Fig. 21a and Fig. 21b, for the constrained and unconstrained problems, respectively. Thus, for both problems the identified classes, represented by the subjects shown in Fig. 22b and Fig. 20c, correspond to a different

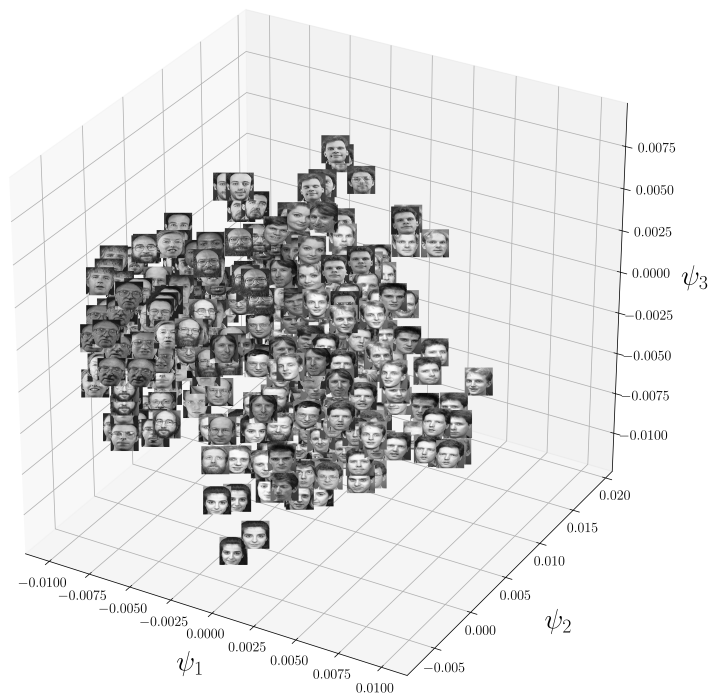


Figure 18: Grassmannian diffusion maps: face images in the training set plus the test face image in the space defined by the first three diffusion coordinates.

subject than the one in the test sample.

The failure of sparse representation in identifying the correct subject using the conventional diffusion maps serves as motivation to the use of the Grassmannian diffusion maps, which is presented next. In this regard, Algorithm 6.1 is used to perform the identification of the test subject presented in Fig. 16. Repeating the same procedure adopted for the conventional diffusion maps, we show in Fig. 23a and in Fig. 23b that the sparse representation method informed by the Grassmannian diffusion maps succeeds in identifying a face image similar to the test sample for both the constrained and unconstrained problems. The identified and test faces are also shown in Fig. 24. Moreover, the residuals for each class k are estimated using Eq. (6.7) to identify the class k that minimizes $r(k)$. From Fig. 25a and Fig. 25b we see that the Grassmannian diffusion maps outperforms the conventional method in this specific case for both l_1 -minimization problems in Eq. (6.5) and Eq. (6.6), respectively. Thus, a correct identification is obtained as shown in Fig. 26.

So far, the identification of a single subject was performed to show the potential of the Grassmannian diffusion maps to inform the sparse representation method used in the facial recognition. Next, the performance of the facial recognition for both the conventional and the Grassmannian diffusion maps is assessed for all 40 subjects in the test set. In this regard, it is worth mentioning that the conventional diffusion maps presented a rather poor performance only identifying 2 subjects when the con-

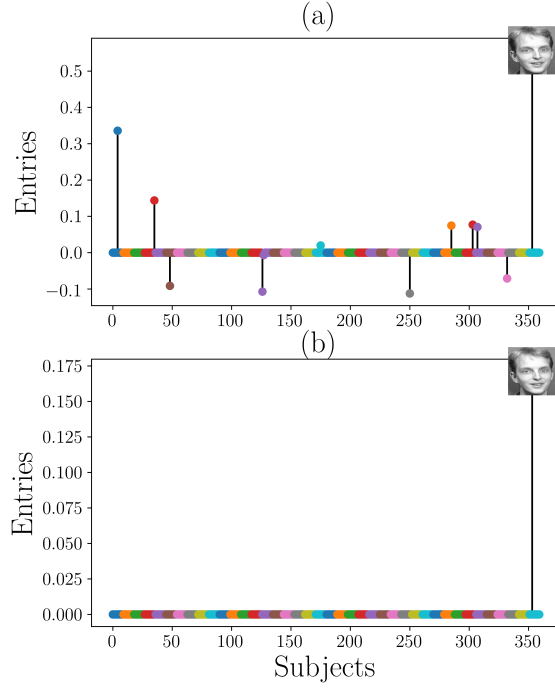


Figure 19: Entries of \mathbf{c} , with colors defining the 40 classes, for the a) constrained and b) unconstrained minimization problems using the conventional diffusion maps.

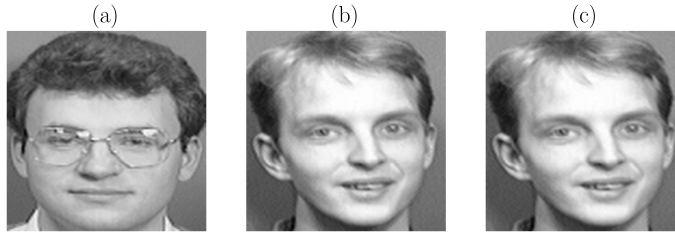


Figure 20: Conventional diffusion maps: a) test face image, and face images identified by the entries of c solving the b) constrained and c) unconstrained minimization problems.

strained minimization is employed, and just 1 subject when solving the unconstrained minimization problem. This poor performance can be justified by the fact that the conventional diffusion maps technique does not identify an underlying subspace structure for the data, and as a consequence the diffusion coordinates will not express this behavior and the test sample will have a higher chance to be represented by a distinct set of face images. On the other hand, the Grassmannian diffusion maps presented high recognition rates; similar, or even superior, to the one obtained using the sparse representation-based classification method, with the difference that the amount of data required to perform the recognition is much smaller. But a direct comparison with the sparse representation-based method is not possible because a different data-

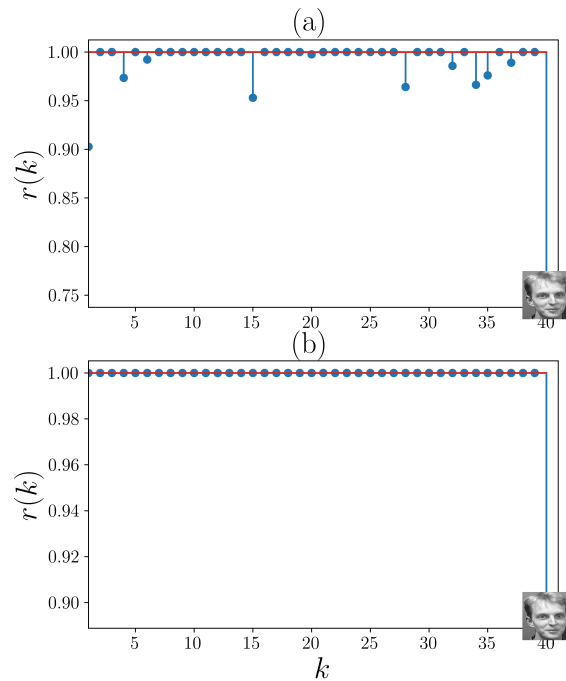


Figure 21: Conventional diffusion maps: residuals $r(k)$ using the constrained a) and unconstrained b) minimization problems.



Figure 22: Conventional diffusion maps: a) test face image, and face images identified by the residuals solving the b) constrained and c) unconstrained minimization problems.

base was utilized in [59]. In this regard, Fig. 27 shows how the recognition rate changes for different values of p defining the dimensionality of the Grassmann manifold $\mathcal{G}(p, n)$. Clearly, one can observe that high recognition rates are obtained even considering $p = 1$, however, in the best case scenario a recognition rate of 95% was achieved for $p = 12, 13$ and 14 . Moreover, it is clear that the recognition rate tends to diminish for very large values of p (i.e., $p > 50$ for instance); however, the use of very larger values of p is not justified in this kind of application. It is worth mentioning that the computational performance of the present technique is comparable with the performance of the sparse representation-based classification method. Only one

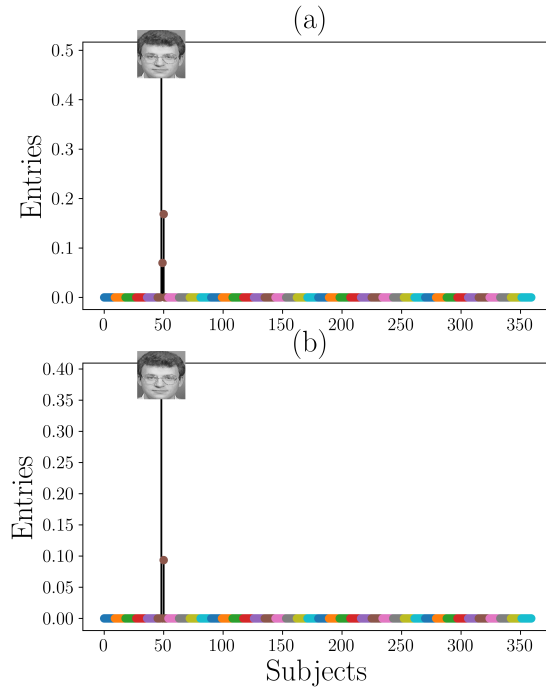


Figure 23: Entries of \mathbf{c} , with colors defining the 40 classes, for the a) constrained and b) unconstrained minimization problems using the Grassmannian diffusion maps.



Figure 24: Grassmannian diffusion maps: a) test face image, and face images identified by the entries of \mathbf{c} solving the b) constrained and c) unconstrained minimization problems.

additional step, the computation of the diffusion coordinates, is introduced.

Concluding remarks. In this paper, a novel dimensionality reduction technique is developed based on the concepts of Grassmann manifold projection and diffusion maps aiming at the characterization and classification of data informed by their intrinsic geometric structure. We demonstrate that an element of a dataset residing in a high-dimensional ambient space can have a representation on a manifold, known as the Grassmann manifold, where its properties are well described by elements of differential geometry. Moreover, the notions of similarity and affinity of elements of a dataset are the key elements to exploit the embedding of the Grassmann manifold on a Euclidean space where the Euclidean metric can be useful for diverse applications

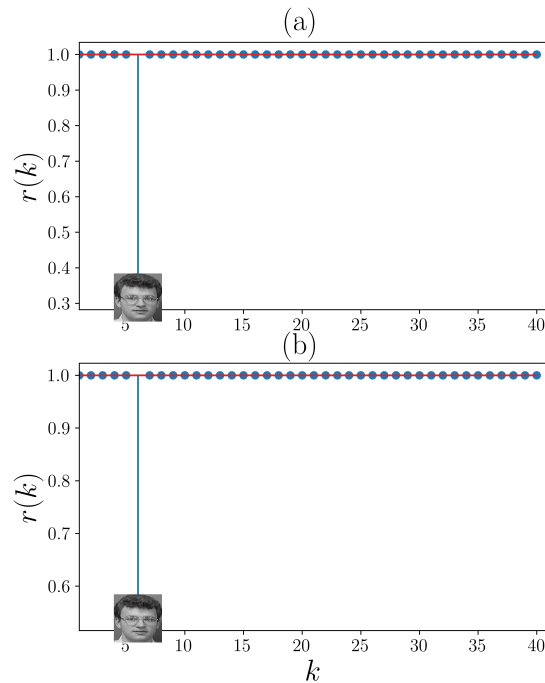


Figure 25: Grassmannian diffusion maps: residuals $r(k)$ using the constrained a) and unconstrained b) minimization problems.



Figure 26: Grassmannian diffusion maps: a) test face image, and face images identified by the residuals solving the b) constrained and c) unconstrained minimization problems.

(e.g., object classification, facial recognition).

The proposed method, Grassmannian diffusion maps, is composed by two main steps, a pointwise dimensionality reduction and a multipoint dimensionality reduction. In the pointwise dimensionality each element of dataset is projected onto a Grassmann manifold where only the most relevant features are kept, and the redundant information are discarded. On the other hand, the multipoint dimensionality reduction consists in the application of the diffusion maps by designing a graph over the Grassmann manifold where a random walk can be performed to reveal the underlying structure connecting the distinct points in the dataset via the eigendecomposition of the transition matrix of the corresponding Markovian process. In comparison

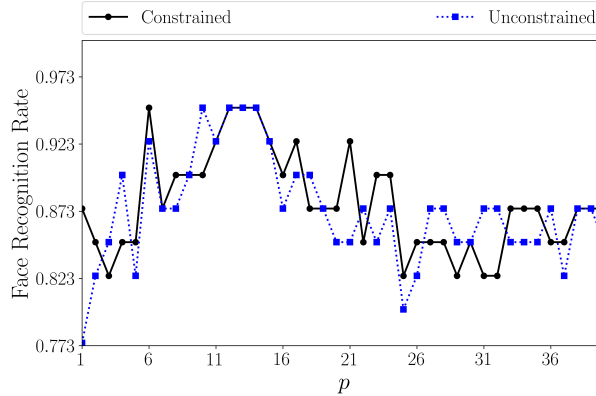


Figure 27: Points in \mathbb{R}^3 colored by their magnitude.

with the conventional diffusion maps, the technique proposed herein uses the intrinsic subset structure of the data to find a geometric connection based on the affinity of these subsets representing points on the Grassmann manifold. Therefore, instead of using the information in the ambient space, which can be more susceptible to data corruption and external factors (e.g., noise, illumination level in images), the Grassmannian diffusion maps circumvent this limitation using the information provided by the underlying lower-dimensional subspace of each data point.

Furthermore, one of the most important elements of the Grassmannian diffusion maps is the selection of an appropriate kernel, defined on the Grassmann manifold, to be used in the context of the Grassmannian diffusion maps. In particular, two lemmas were presented and proved to show the behavior of the first order statistics of the off-diagonal entries of the Grassmannian kernel with changes in its dimensionality. It was demonstrated that the expected value of the off-diagonal entries of the projection kernel grows with order $\mathcal{O}(p^2)$, whereas the expected value off-diagonal elements of the Binet-Cauchy kernel decrease drastically with upper bound in the order $\mathcal{O}(p^p)$, if $p < n/2$; and grows at a high rate with upper bound in the order $\mathcal{O}((n-p)^{(n-p)})$, otherwise.

The performance of the Grassmannian diffusion maps is assessed in three examples where comparison with the conventional diffusion maps are performed to show the potential of this novel approach. In this regard, the first example contained a theoretical experiment to verify the ability of the present method in finding a structured connection among points projected on the Grassmann manifold represented by the unit circle in \mathbb{R}^3 . It was shown that the Grassmannian diffusion maps outperforms the conventional method in identifying a well-defined parametric structure of the data when they are projected on the Grassmann manifold $\mathcal{G}(1, 3)$ and it can be explained by the capability of the Grassmannian diffusion maps in identify the underlying subspace associated with each element in the dataset.

The second example presented an experiment with high-dimensional random field data where the Grassmann manifold is used to identify the most relevant feature of the data influencing their clustering. In this example, the data is formed by a composition of matrices defined by oscillatory functions where the underlying geometric structure is mainly defined by their frequency than by the phase shift. Therefore, the Grassmannian diffusion maps was able to use this information to cluster the points

with same frequency in the same position in the diffusion space, and this structure was easily identified using a clustering algorithm in the diffusion coordinates, such as k-means.

The third example presented a practical application of two techniques developed herein, the Grassmannian diffusion maps and the Grassmannian diffusion maps-based data classification using sparse representation. It was demonstrated using the AT&T Database of Faces (AT&T Laboratories Cambridge) that the Grassmannian diffusion maps outperforms the conventional method in identifying 40 face images subject to varying illumination conditions, change in face expressions, and occurrence of occlusions. Moreover, the present technique has the advantage to present high recognition rates (95% in the best-case scenario) using a fraction of the information used by conventional face recognition techniques based on sparse representation.

Acknowledgements. This work has been supported by the U.S. Department of Energy under grant number DE-SC0020428 and by internal funds provided by Johns Hopkins University.

REFERENCES

- [1] P.-A. ABSIL, A. EDELMAN, AND P. KOEV, *On the largest principal angle between random subspaces*, Linear Algebra and its Applications, 414 (2006), pp. 288 – 294.
- [2] L. AUSLANDER AND R. MACKENZIE, *Introduction to Differentiable Manifolds*, Dover Books on Mathematics, Dover Publications, 2012.
- [3] M. BALASUBRAMANIAN AND E. L. SCHWARTZ, *The isomap algorithm and topological stability*, Science, 295 (2002), pp. 7–7, <https://doi.org/10.1126/science.295.5552.7a>.
- [4] N. H. BALOV, *Comparing random variables on manifolds*, in 2008 Joint Statistical Meetings, 2008.
- [5] R. G. BARANIUK, V. CEVHER, AND M. B. WAKIN, *Low-dimensional models for dimensionality reduction and signal recovery: A geometric perspective*, Proceedings of the IEEE, 98 (2010), pp. 959–971.
- [6] E. BEGELFOR AND M. WERMAN, *Affine invariance revisited*, in 2006 IEEE Computer Society Conference on Computer Vision and Pattern Recognition (CVPR’06), vol. 2, 2006, pp. 2087–2094.
- [7] P. N. BELHUMEUR, J. P. HESPANHA, AND D. J. KRIEGMAN, *Eigenfaces vs. fisherfaces: recognition using class specific linear projection*, IEEE Transactions on Pattern Analysis and Machine Intelligence, 19 (1997), pp. 711–720.
- [8] M. BELKIN AND P. NIYOGI, *Laplacian eigenmaps for dimensionality reduction and data representation*, Neural Computation, 15 (2003), pp. 1373–1396.
- [9] E. J. CANDÈS, X. LI, Y. MA, AND J. WRIGHT, *Robust principal component analysis?*, Journal of the ACM, 58 (2011), p. 1–37.
- [10] X. CHEN AND Y. YANG, *Diffusion k-means clustering on manifolds: Provable exact recovery via semidefinite relaxations*, Applied and Computational Harmonic Analysis, (2020), <https://doi.org/10.1016/j.acha.2020.03.002>.
- [11] R. R. COIFMAN, I. G. KEVREKIDIS, S. LAFON, M. MAGGIONI, AND B. NADLER, *Diffusion maps, reduction coordinates, and low dimensional representation of stochastic systems*, Multi-scale Modeling & Simulation, 7 (2008), pp. 842–864, <https://doi.org/10.1137/070696325>.
- [12] R. R. COIFMAN AND S. LAFON, *Diffusion maps*, Applied and Computational Harmonic Analysis, 21 (2006), pp. 5 – 30, <https://doi.org/https://doi.org/10.1016/j.acha.2006.04.006>. Special Issue: Diffusion Maps and Wavelets.
- [13] H. COURANT, R. COURANT, C. COURANT, H. ROBBINS, I. STEWART, AND P. ROBBINS, *What is Mathematics?: An Elementary Approach to Ideas and Methods*, Oxford paperbacks : Mathematics / Oxford paperbacks, Oxford University Press, 1996.
- [14] M. P. DO CARMO, *Riemannian Geometry*, Mathematics (Boston, Mass.), Birkhäuser, 1992.
- [15] D. L. DONOHO AND C. GRIMES, *Hessian eigenmaps: Locally linear embedding techniques for high-dimensional data*, Proceedings of the National Academy of Sciences, 100 (2003), pp. 5591–5596, <https://doi.org/10.1073/pnas.1031596100>.
- [16] K. R. DOS SANTOS, O. BRUDASTOVA, AND I. A. KOUGIOUMTZOGLU, *Spectral identification of nonlinear multi-degree-of-freedom structural systems with fractional derivative terms based*

- on incomplete non-stationary data, *Structural Safety*, 86 (2020), p. 101975.
- [17] A. EDELMAN AND N. R. RAO, *Random matrix theory*, *Acta Numerica*, 14 (2005), p. 233–297.
- [18] C. GAN, J. MAO, Z. ZHANG, AND Q. ZHU, *A tensor compression algorithm using tucker decomposition and dictionary dimensionality reduction*, *International Journal of Distributed Sensor Networks*, 16 (2020), p. 1550147720916408.
- [19] X. GENG, D.-C. ZHAN, AND Z.-H. ZHOU, *Supervised nonlinear dimensionality reduction for visualization and classification*, *IEEE Transactions on Systems, Man, and Cybernetics, Part B (Cybernetics)*, 35 (2005), pp. 1098–1107.
- [20] D. GIOVANIS AND M. SHIELDS, *Uncertainty quantification for complex systems with very high dimensional response using grassmann manifold variations*, *Journal of Computational Physics*, 364 (2018), pp. 393 – 415, <https://doi.org/https://doi.org/10.1016/j.jcp.2018.03.009>.
- [21] D. G. GIOVANIS AND M. D. SHIELDS, *Data-driven surrogates for high dimensional models using gaussian process regression on the grassmann manifold*, 2020, <https://arxiv.org/abs/2003.11910>.
- [22] P. GRIFFITHS AND J. HARRIS, *Complex Algebraic Varieties*, John Wiley & Sons, 2011, ch. 1, pp. 128–211.
- [23] A. GU, F. SALA, B. GUNEL, AND C. RÉ, *Learning mixed-curvature representations in product spaces*, in *International Conference on Learning Representations*, 2019.
- [24] J. HAMM AND D. D. LEE, *Grassmann discriminant analysis: A unifying view on subspace-based learning*, in *Proceedings of the 25th International Conference on Machine Learning, ICML '08*, New York, NY, USA, 2008, Association for Computing Machinery, p. 376–383, <https://doi.org/10.1145/1390156.1390204>.
- [25] J. HAMM AND D. D. LEE, *Extended grassmann kernels for subspace-based learning*, in *Advances in Neural Information Processing Systems 21*, D. Koller, D. Schuurmans, Y. Bengio, and L. Bottou, eds., Curran Associates, Inc., 2009, pp. 601–608.
- [26] M. HARANDI, R. HARTLEY, C. SHEN, B. LOVELL, AND C. SANDERSON, *Extrinsic methods for coding and dictionary learning on grassmann manifolds*, *International Journal of Computing Vision*, 114 (2015), p. 113–136, <https://doi.org/https://doi.org/10.1007/s11263-015-0833-x>.
- [27] M. T. HARANDI, M. SALZMANN, S. JAYASUMANA, R. HARTLEY, AND H. LI, *Expanding the family of grassmannian kernels: An embedding perspective*, 2014, <https://arxiv.org/abs/1407.1123>.
- [28] P. HARTMAN, *On the local uniqueness of geodesics*, *American Journal of Mathematics*, 72 (1950), pp. 723–730.
- [29] X. HE, S. YAN, Y. HU, P. NIYOGI, AND H.-J. ZHANG, *Face recognition using laplacianfaces*, *IEEE Transactions on Pattern Analysis and Machine Intelligence*, 27 (2005), pp. 328–340.
- [30] J. E. HURTADO, *Dimensional reduction and data compression*, in *Structural Reliability*, J. E. Hurtado, ed., vol. 17, Springer, Berlin, Heidelberg, 2004. *Lecture Notes in Applied and Computational Mechanics*.
- [31] I. JOLLIFFE, *Principal Component Analysis*, Springer Berlin Heidelberg, 2011, pp. 1094–1096, https://doi.org/10.1007/978-3-642-04898-2_455.
- [32] A. KOLMOGOROV, *Foundations of the Theory of Probability*, Martino Fine Books, 2013.
- [33] I. A. KOUGIOUMTZOGLU, K. R. DOS SANTOS, AND L. COMERFORD, *Incomplete data based parameter identification of nonlinear and time-variant oscillators with fractional derivative elements*, *Mechanical Systems and Signal Processing*, 94 (2017), pp. 279 – 296.
- [34] I. A. KOUGIOUMTZOGLU, I. PETROMICHELAKIS, AND A. F. PSAROS, *Sparse representations and compressive sampling approaches in engineering mechanics: A review of theoretical concepts and diverse applications*, *Probabilistic Engineering Mechanics*, 61 (2020), p. 103082.
- [35] L.-H. LIM, K. SZE-WAI WONG, AND K. YE, *Numerical algorithms on the affine grassmannian*, *SIAM Journal on Matrix Analysis and Applications*, 40 (2019), pp. 371–393, <https://doi.org/10.1137/18M1169321>.
- [36] S. P. LLOYD, *Least squares quantization in pcm*, *IEEE Transactions on Information Theory*, 28 (1982), pp. 129–137.
- [37] J. MARUSKIN, *Introduction to Dynamical Systems and Geometric Mechanics*, Solar Crest Publishing, LLC, 2012.
- [38] J. MIAO AND A. BEN-ISRAEL, *On principal angles between subspaces in m* , *Linear Algebra and its Applications*, 171 (1992), pp. 81 – 98.
- [39] K. R. MOON, J. S. STANLEY, D. BURKHARDT, D. VAN DIJK, G. WOLF, AND S. KRISHNASWAMY, *Manifold learning-based methods for analyzing single-cell rna-sequencing data*, *Current Opinion in Systems Biology*, 7 (2018), pp. 36 – 46.
- [40] K. R. MOON, D. VAN DIJK, Z. WANG, W. CHEN, M. J. HIRN, R. R. COIFMAN, N. B.

- IVANOVA, G. WOLF, AND S. KRISHNASWAMY, *Phate: A dimensionality reduction method for visualizing trajectory structures in high-dimensional biological data*, bioRxiv, (2017), <https://doi.org/10.1101/120378>, <https://arxiv.org/abs/https://www.biorxiv.org/content/early/2017/03/24/120378.full.pdf>.
- [41] C. MU, Y. ZHANG, J. WRIGHT, AND D. GOLDFARB, *Scalable robust matrix recovery: Frank-wolfe meets proximal methods*, SIAM Journal on Scientific Computing, 38 (2016), pp. A3291–A3317.
- [42] R. J. MUIRHEAD, *Aspects of multivariate statistical theory*, John Wiley & Sons, 1982.
- [43] A. OLIVIER, D. GIOVANIS, B. AAKASH, M. CHAUHAN, L. VANDANAPU, AND M. SHIELDS, *Uqpy: A general purpose python package and development environment for uncertainty quantification*, Journal of Computational Science, (2020), p. 101204.
- [44] J. OPREA, *Differential Geometry and Its Applications*, Classroom resource materials, Mathematical Association of America, 2007.
- [45] S. T. ROWEIS AND L. K. SAUL, *Nonlinear dimensionality reduction by locally linear embedding*, Science, 290 (2000), pp. 2323–2326, <https://doi.org/10.1126/science.290.5500.2323>.
- [46] B. SCHÖLKOPF, A. SMOLA, AND K. MÜLLER, *Nonlinear component analysis as a kernel eigenvalue problem*, Neural Computation, 10 (1998), pp. 1299–1319.
- [47] C. SOIZE AND R. GHANEM, *Probabilistic learning on manifolds*, 2020, <https://arxiv.org/abs/2002.12653>.
- [48] S. SOMMER, T. FLETCHER, AND X. PENNEC, *1 - introduction to differential and riemannian geometry*, in Riemannian Geometric Statistics in Medical Image Analysis, X. Pennec, S. Sommer, and T. Fletcher, eds., Academic Press, 2020, pp. 3 – 37.
- [49] I. STANKOVIĆ, *Recovery of images with missing pixels using a gradient compressive sensing algorithm*, 2014, <https://arxiv.org/abs/1407.3695>.
- [50] J. B. TENENBAUM, V. D. SILVA, AND J. C. LANGFORD, *A global geometric framework for nonlinear dimensionality reduction*, Science, 290 (2000), pp. 2319–2323, <https://doi.org/10.1126/science.290.5500.2319>.
- [51] P. TURAGA, A. VEERARAGHAVAN, AND R. CHELLAPPA, *Statistical analysis on stiefel and grassmann manifolds with applications in computer vision*, in 2008 IEEE Conference on Computer Vision and Pattern Recognition, 2008, pp. 1–8.
- [52] M. A. TURK AND A. P. PENTLAND, *Face recognition using eigenfaces*, in Proceedings. 1991 IEEE Computer Society Conference on Computer Vision and Pattern Recognition, 1991, pp. 586–591.
- [53] J. UH, M. A. KHAN, AND C. HUA, *Four-dimensional MRI using an internal respiratory surrogate derived by dimensionality reduction*, Physics in Medicine and Biology, 61 (2016), pp. 7812–7832.
- [54] L. J. P. VAN DER MAATEN AND G. E. HINTON, *Visualizing data using t-sne*, Journal of Machine Learning Research, 9 (2008), p. 2579–2605.
- [55] S. VISHWANATHAN AND A. SMOLA, *Binet-cauchy kernels. advances in neural information processing systems*, in Advances in Neural Information Processing Systems, no. 17 in NIPS '04, 2004.
- [56] B. WANG, Y. HU, J. GAO, Y. SUN, AND B. YIN, *Low rank representation on grassmann manifolds: An extrinsic perspective*, 2015, <https://arxiv.org/abs/1504.01807>.
- [57] R. WANG, X. WU, AND J. KITTLER, *Graph embedding multi-kernel metric learning for image set classification with grassmann manifold-valued features*, IEEE Transactions on Multimedia, (2020), pp. 1–1.
- [58] Y.-C. WONG, *Differential geometry of grassmann manifolds*, in Proceedings of the National Academy of Sciences of the United States of America, 1967, p. 589–594.
- [59] J. WRIGHT, A. Y. YANG, A. GANESH, S. S. SASTRY, AND Y. MA, *Robust face recognition via sparse representation*, IEEE Transactions on Pattern Analysis and Machine Intelligence, 31 (2009), pp. 210–227.
- [60] J. WU, L. HUANG, W. LI, H. CHAN, C. LIU, AND R. GAU, *Sparse subspace clustering with linear subspace-neighborhood-preserving data embedding*, in 2020 IEEE 11th Sensor Array and Multichannel Signal Processing Workshop (SAM), 2020, pp. 1–5.
- [61] W. YAN, Q. SUN, H. SUN, AND Y. LI, *Joint dimensionality reduction and metric learning for image set classification*, Information Sciences, 516 (2020), pp. 109 – 124.
- [62] K. YE AND L.-H. LIM, *Schubert varieties and distances between subspaces of different dimensions*, 2014, <https://arxiv.org/abs/1407.0900>.
- [63] K. YE, K. S.-W. WONG, AND L.-H. LIM, *Optimization on flag manifolds*, 2019, <https://arxiv.org/abs/1907.00949>.
- [64] J. ZHANG, G. ZHU, R. W. H. JR., AND K. HUANG, *Grassmannian learning: Embedding geometry awareness in shallow and deep learning*, 2018, <https://arxiv.org/abs/1808.02229>.

- [65] R. ZIMMERMANN, *Manifold interpolation and model reduction*, 2019, <https://arxiv.org/abs/1902.06502>.